Mass, Nutrients and DOC lateral transports off Northwest Africa during fall 2002 and spring 2003

Nadia Burgoa[1], Francisco Machín[1], Ángeles Marrero-Díaz[1], Ángel Rodríguez-Santana[1], Antonio Martínez-Marrero[2], Javier Arístegui[2], and Carlos M. Duarte[3]

[1]Departamento de Física, Universidad de Las Palmas de Gran Canaria, Spain
[2]Instituto de Oceanografía y Cambio Global, Universidad de Las Palmas de Gran Canaria, Spain
[3]Red Sea Research Center, King Abdullah University of Science and Technology, Saudi Arabia

Correspondence: Nadia Burgoa (nadia.burgoa@ulpgc.es)

Abstract.

The circulation patterns and the impact of lateral export of nutrients and organic matter off NW Africa are examined by applying an inverse model to two hydrographic datasets gathered in fall 2002 and spring 2003. These estimates show significant changes in the circulation patterns at central levels from fall to spring, particularly in the southern boundary of the domain
5 related to zonal shifts of the Cape Verde Frontal Zone. Southward transports at surface and central levels at 26°N are 5.6±1.9 Sv in fall that increase to 6.7±1.6 Sv in spring; westward transports at 26°W are 6.0±1.8 Sv in fall to weaken to 4.0±1.8 Sv in spring; at 21°N a remarkable temporal variability is obtained, with a northward mass transport of 4.4±1.5 Sv in fall and a southward 5.2±1.6 Sv in spring. At intermediate levels important spatio-temporal differences are also observed, where it must be highlighted a northward net mass transport of 2.0±1.9 Sv obtained in fall at both the south and north transects.
10 The variability in the circulation patterns is also reflected in lateral transports of inorganic nutrients (SiO_2, NO_3, PO_4) and dissolved organic carbon (DOC). Hence, in fall the area acts as a sink of inorganic nutrients and a source of DOC, while in spring it reverses to a source of inorganic nutrients and a sink of DOC. A comparison between nutrient fluxes from both *in situ* observations and numerical modelling output is finally addressed.

1 INTRODUCTION

15 The North Atlantic Subtropical Gyre (NASG) is one of the most important components in the thermohaline circulation. It presents a well-known intensification in its western margin, the Gulf Stream, with maximum velocities up to 2 m s^{-1} (Halkin et al., 1985). The currents observed in this western margin of the gyre occupy a small horizontal extension as compared to that of the currents in the eastern side, resulting in an asymmetric gyre (Stramma, 1984; Tomczak and Godfrey, 2003). The low intensity of the currents at the eastern boundary made them very little studied until the 1970s, when CINECA
20 (Cooperative Investigations of the Northern Part of the Eastern Central Atlantic) program focused on the productive African upwelling system (Ekman, 1923; Tomczak, 1979; Hughes and Barton, 1974; Hempel, 1982). Käse and Siedler (1982) found striking intense currents south of the Azores connected to the Gulf Stream and suggested that part of the recirculation of the NASG occurs southward in the vicinity of the African coast. Later on, several surveys based on both *in situ* and remote

sensing observations contributed to define the general characteristics for the average flow of the region (Käse and Siedler, 1982; Stramma, 1984; Käse et al., 1986; Stramma and Siedler, 1988; Mittelstaedt, 1991; Zenk et al., 1991; Fiekas et al., 1992; Hernández-Guerra et al., 1993).

Most of the eastward flow from the Gulf Stream is confined to a band between the Azores and Madeira Islands, recirculating southward through the Canary Islands and north of the Cape Verde Islands to become into a southwestward flow (Stramma, 1984). This current system is composed by the Azores Current (AC), the Canary Current (CC), the Canary Upwelling Current (CUC), the North Equatorial Current (NEC) and the Poleward Undercurrent (PUC). The AC divides into several branches defining the boundary current system off Northwest Africa. It firstly feeds the Iberian Current (Haynes et al., 1993) while a second significant branch enters the Mediterranean Sea (Candela, 2001). Most of the AC recirculates southward splitting into the main CC across the Canarian archipelago and the secondary CUC (Pelegrí et al., 2005, 2006). These currents extend southward developing the Cape Verde Frontal Zone (CVFZ), a density-compensated front with North Atlantic Central Water at its northern side and South Atlantic Central Water at its southern one (Zenk et al., 1991; Martínez-Marrero et al., 2008). Finally, the PUC is located below the CUC flowing northward on the continental slope (Barton, 1989; Machín and Pelegrí, 2009; Machín et al., 2010; Pelegrí and Peña-Izquierdo, 2015).

The mesoscale activity constitutes a second main feature in the area of interest, which might be even more energetic than the average flow itself (Sangrà et al., 2009). Three mesoscale domains may be defined: the Canary Eddy Corridor (CEC, Sangrà et al. (2009)), the CVFZ and the upwelling front. The CEC is located downstream of the Canary Islands where the interaction between the southward flow and the archipelago generates long-lived eddies (Arístegui et al., 1994; Barton et al., 1998; Sangrà et al., 2007, 2009; Ruiz et al., 2014; Barceló-Llull et al., 2017a). The second mesoscale domain is the CVFZ, where several meanders and eddies produce strong interleaving between the water masses involved (Pérez-Rodríguez et al., 2001; Martínez-Marrero et al., 2008). In this domain, the CC and the CUC separate from the African coast fueling the NEC, giving rise to a shadow zone featured by poorly ventilated waters (Luyten et al., 1983). The third area is the front arising between the coastal upwelled waters and the stratified interior waters, defining the Eastern Boundary Upwelling System (EBUS) in the Northwest African region (Mittelstaedt, 1983; Pastor et al., 2008; Arístegui et al., 2009). This EBUS is actually located off the African slope from the Gulf of Cadiz until Cape Blanc/Cape Verde in summer/winter with a high mesoscale variability in the form of both filaments and eddies (Hagen, 2001; Sangrà et al., 2009; Ruiz et al., 2014). The upwelling process raises nutrient-rich waters to the euphotic layer, developing a high primary production latitudinal band off Northwest Africa known as the Coastal Transition Zone (CTZ) (Barton et al., 1998; Pelegrí et al., 2006). These mesoscale features play an essential role as a lateral source of organic matter towards the oligotrophic waters of the NASG (Barton et al., 1998; García-Muñoz et al., 2004, 2005; Pelegrí et al., 2006; Álvarez-Salgado et al., 2007; Sangrà et al., 2009).

The distribution of inorganic nutrients and organic matter in the ocean responds to a combined effect of physical and biogeo-chemical processes. Within the euphotic zone, primary production is solely limited by the availability of inorganic nutrients (IN) (Copin-Montegut and Copin-Montegut, 1983; Falkowski et al., 1998). Below the euphotic zone respiration exceeds primary production. As a result, the organic matter produced at the sea surface is remineralized in the subsurface layers and hence

the concentration of IN increases from the interplay between the local rate of remineralization and the rate of water supply (Azam, 1998; Del Giorgio and Duarte, 2002; Pelegrí et al., 2006; Pelegrí and Benazzouz, 2015b).

In order to study the impact of lateral transports on the distributions of biogeochemical variables, the first step to follow is to analyze the dynamic of the area with an inverse box model. This method provides a velocity field consistent with both mass and properties conservation within a closed volume and with the thermal wind equation (Wunsch, 1996). Several authors have already described the circulation patterns of the NASG by applying an inverse model (Ganachaud and Wunsch, 2002; Ganachaud, 2003b, a; Hernández-Guerra et al., 2005; Machín et al., 2006; Pérez-Hernández et al., 2013; Hernández-Guerra et al., 2017). Moreover, some recent manuscripts addressing lateral advective transports of biogeochemical variables have shed light on this topic in the EBUS off NW Africa (Álvarez and Álvarez-Salgado, 2009; Alonso-González et al., 2009; Santana-Falcón et al., 2017; Fernández-Castro et al., 2018).

To sum up, the main goal of this manuscript is to present an *in situ* hydrographic database and to estimate lateral mass, IN and DOC transports during fall and spring seasons south of the Canary Islands in the context of a highly variable environment featured by the Canary Eddy Corridor, the upwelling off Northwest African and the CVFZ. The remaining of this manuscript is organized as follows: the dataset is presented in section 2; the seasonal distribution of the water masses and their properties is displayed in section 3; the technical details of the inverse box model are covered in section 4; the resulting velocity field and the corresponding mass, nutrient and organic matter transports are presented in section 5. Section 6 is devoted to the discussion to end up with some conclusions at section 7.

2   DATASET

COCA-I and COCA-II cruises were carried out in fall (10 September to 1 October 2002) and spring (21 May to 7 June 2003) respectively, aboard the BIO Hesperides as part of the research project Coastal-Ocean Carbon Exchange in the Canary Region (Hernández-León et al., 2019). The location of Conductivity-Temperature-Depth (CTD), inorganic nutrients (IN) and dissolved organic carbon (DOC) stations in COCA-I and COCA-II defines a closed box along three transects (Fig. 1). The northern transect (N) spans from station 1 to 32 at 26°N (section from stations 1 to 11 is tilted some 30° with respect to the east). The western transect (W) is located at 26°W from station 32 to 42. Finally, the southern zonal transect (S) at 21°N runs from station 42 to 63 (COCA-I) or 66 (COCA-II) over the continental slope (Tab. 1). The distance between neighbouring CTD stations was some 50 km except for the stations over the continental slope where this distance was shortened. Adjacent DOC and IN stations were separated by a variable distance, with its lowest value being about 50 km at stations closer to the coast.

CTD data were collected from the sea surface down to 2000 m depth with a vertical resolution of 2 dbar. *In situ* temperature was calibrated with 45 readings performed with a reversible digital thermometer, while salinity was calibrated by analysing 60 water samples with the Portasal salinometer. The residuals have an average value of $0.00013 \pm 0.00400\,°C$ and 0.0005 ± 0.005 in salinity.

DOC was measured with a total organic carbon (TOC) analyzer (Shimadzu TOC-5000), assuming that almost all TOC was in dissolved form. Water samples (10 mL) were dispensed directly into glass ampoules, previously combusted at 500 °C

during 12 h. 50 µL of H_3PO_4 were added immediately to the sample, sealed and stored at 4 °C until analysed. Before the analysis, samples were sparged with CO_2-free air for several minutes to remove inorganic carbon. TOC concentrations were determined from standard curves (30 to 200 µM) of potassium hydrogen phthalate produced every day (Thomas et al., 1995). To check accuracy and precision, reference material from Jonathan H. Sharp laboratory (University of Delaware) was analysed daily. DOC distribution up to 2000 m depth presented a more representative coverage in fall than in spring (Fig. 2, green dots), despite in spring the number of stations was higher than in fall (Fig. 1, black circles; Tab. 1).

The three inorganic nutrient sampled were silicates (SiO_2), nitrates plus nitrites (NO_x), and phosphates (PO_4). These samples were frozen until measured with a Bran Luebe AA3 autoanalyser following the standard methodology established by Hansen and Koroleff (1999). Nutrient data covered up to 2000 m, while in fall they concentrated in the shallowest layers ($<$ 200 m, Fig. 2, pink crosses).

Wind data were selected from the QuikSCAT database made available by CERSAT (Centre ERS d' Archivage et de Traitement, http://www.ifremer.fr/cersat/). These wind fields were averaged weekly with a spatial resolution of 0.5° (shown in Fig. 1 with half of the original spatial resolution). The Smith-Sandwell database with 1-minute horizontal resolution was used as the source of bathymetry data (Smith and Sandwell, 1997).

Freshwater flux data were estimated from the rates of evaporation and precipitation extracted from the Surface Marine Data 1994 of Da Silva (http://iridl.ldeo.columbia.edu/SOURCES/.DASILVA/.SMD94/). The climatological mean depths of the neutral density field for the years 2002 and 2003 were calculated from the climatological temperature and salinity extracted from the World Ocean Atlas 2013 (WOA13, https://www.nodc.noaa.gov/OC5/woa13/woa13data.html).

GLORYS (GLOBAL_REANALYSIS_PHY_001_025 product) issued by Copernicus Marine Environment Monitoring Service (CMEMS, http://marine.copernicus.eu) was used as a primary source of dynamic variables. Its horizontal resolution is 1/12° with 50 standard depths. Hydrological data from GLORYS were also employed to diagnose the average oceanographic conditions during each cruise. This product assimilates field observations in real time.

SEALEVEL_GLO_PHY_L4_REP_OBSERVATIONS_008_047 product provided surface geostrophic currents estimated from sea level anomalies. These data capture the mesoscale structures and are helpful to validate the near-surface geostrophic field estimated from the inverse model.

GLORYS-BIO (GLOBAL_REANALYSIS_BIO_001_029 product) produced daily mean 3D biogeochemical fields with the same resolution as GLORYS. This reanalysis forces the biogeochemical model with the nutrient initial conditions from WOA13. IN concentrations from GLORYS-BIO (SiO_2, NO_3, and PO_4) were used to assess nutrient transports by the model (in section 5).

The data treatment, the graphical representations and the inverse model are coded in MATLAB (MATLAB, 2018). The vertical sections are produced using the 'nearest' 2D interpolations, a method also employed in the estimates of the IN and DOC transports. Ocean Data View using the DIVA gridding method is employed to produce DOC concentration charts (Schlitzer, Reiner, 2019).

3   HYDROGRAPHY AND WATER MASSES

125   Neutral density $\gamma_n = \gamma_n(\theta, S, p)$ is used as the density reference variable, being the isoneutrals the surfaces where the values of γ_n are constant (Jackett and McDougall, 1997). The γ_n vertical sections contain the surface (SW), central (CW), intermediate (IW) and deep water (DW) masses according to Macdonald (1998) for the North Atlantic at 24°N, represented with white dashed lines at 26.44, 27.38 and 27.82 $\mathrm{kg\,m^{-3}}$ (Fig. 2). The x-axis direction is selected according to the path followed by the vessel during both cruises, starting in the northeast and finishing in the southeast of the domain. The N/W and W/S corners are

130   indicated with two vertical grey dashed lines at stations 32 and 42, respectively.

The $\Theta - S_A$ diagrams exhibit four regions delimited by potential density anomaly contours of 26.39, 27.30 and 27.72 $\mathrm{kg\,m^{-3}}$, equivalent to the isoneutrals which separate the main water masses (Fig. 3). These three isoneutrals are approximately at 132/123, 672/700 and 1294/1305 m depth (Fig. 2). The water masses sampled during both cruises are North Atlantic Central Water (NACW), South Atlantic Central Water (SACW), Antarctic Intermediate Water (AAIW), Mediterranean Water (MW),

135   and North Atlantic Deep Water (NADW) (Emery and Meincke, 1986; Macdonald, 1998; Emery, 2008). Their main hydrological characteristics are summarized in Table 2. Below the mixing layer and above 700 m ($26.44 < \gamma_n < 27.38 \ \mathrm{kg\,m^{-3}}$), NACW and SACW are the dominant water masses. SACW is featured by a higher amount of nutrients, $1 - 2 \ °\mathrm{C}$ colder and $0.1 - 0.4$ fresher than NACW (Fig. 3 and Tab. 2). Below, from 700 up to 1300 m ($27.38 < \gamma_n < 27.82 \ \mathrm{kg\,m^{-3}}$), the intermediate waters AAIW and MW are the dominant water masses (Hernández-Guerra et al., 2017). MW is a relatively warm and salty water

140   mass, while AAIW is colder and fresher (Tab. 2). Finally, below 1300 m ($\gamma_n > 27.82 \ \mathrm{kg\,m^{-3}}$) the predominant water mass is NADW with *in situ* temperature and salinity values lower than $5.7 \ °\mathrm{C}$ and 35.14 (Tab. 2).

A description about the temporal variability of the water masses is also performed with observations from the $\Theta - S_A$ diagrams (Fig. 3). The distribution of water masses is quite similar for both cruises. There is a higher temperature variability at surface waters during fall with maximum values ~~2-3ºC~~ 2-3 ºC higher than in spring. During spring, the variability observed

145   at central waters is associated to larger fluctuations in salinity affecting the whole water column. At DW there is a higher contribution of NADW in the whole domain during fall. Finally, the surface layer is thicker in fall than in spring in all the sections made with respect to γ_n.

These temporal differences may also be described transect to transect. The northern transect (Fig. 2, stations 2 to 32; Fig. 3, margenta dots) is occupied by NACW, AAIW, MW and NADW in both seasons. At intermediate levels, a higher contribution

150   of MW is observed in spring while a slightly higher contribution of AAIW is obtained in fall. The western transect (Fig. 2, stations 32 to 42; Fig. 3, dark grey dots) has a similar distribution as the northern one, with a lower variability in the upper layers and a smaller influence of MW. In the southern transect (Fig. 2, stations 42 to $63 - 66$; Fig. 3, blue dots), the highest spatio-temporal variability is observed. This variability at surface and central levels is associated to the position of the CVFZ and, in turn, to the meso- and submesoscale structures associated to the front. The CVFZ is located where the isohaline of 36,

155   or equivalently $S_A = 36.15 \ \mathrm{g\,kg^{-1}}$, intersects the 150 m isobath (Zenk et al., 1991) (Fig. 4). CVFZ is found in the southern transect in its westernmost position in fall, at stations $46 - 48$. Hence, SACW with relatively low S_A is observed above the upper limit of CW east of the CVFZ location (Fig. 4). In spring, the CVFZ shifts to a position closer to the African coast at

station 52, with a water incursion of higher salinity NACW centred at station 58 (Figs. 4 and 5). At intermediate levels, MW is registered at the northern transect while in the southern one the predominant water mass is AAIW. Regarding the seasonal variability, the contribution of MW in the northern transect is higher in spring while the contribution of AAIW in the southern transect is higher in fall.

Although the IN have been extracted from the model and the distributions of Θ, S_A and γ_n have been obtained from the hydrographic observations, there is a good agreement between the structures described by both datasets. The *in situ* concentrations of SiO_2, NO_X and PO_4 up to 250 m depth (black dots in Fig. 6) are represented together with the time-averaged concentrations of SiO_2, NO_3 and PO_4 up to 2000 m depth selected from GLORYS-BIO. In this way the IN outputs from the model are compared with *in situ* observations since their concentration in both cases present an acceptable match with the exception of NO_X and PO_4 concentrations at the S transect. On the other hand, the IN model outputs look alike IN from historical *in situ* databases (not shown here).

At central levels, high IN concentrations have been sampled near the continental slope in both the northern (stations 10 to 18) and southern (50 to 56) transects in fall. Values observed are 1-5 $\mu mol\,kg^{-1}$ for NO_3 and 0.1-0.4 $\mu mol\,kg^{-1}$ for PO_4 higher values than those recorded in spring at similar places (Fig. 7). This might be related to long-lived mesoscale eddies or instabilities related to the CVFZ (Zenk et al., 1991; Sangrà et al., 2009). IN concentrations are notably high at intermediate and deep levels as compared to those at central levels (Fig. 6) and have the same order of magnitude as those documented before in the domain (Pérez et al., 2001; Pérez-Hernández et al., 2013). The distributions of SiO_2, NO_3 and PO_4 are similar in both cruises and their concentrations increase with depth as a result of the remineralization of organic matter (Fig. 7). The area where the least nutrients are found at depth throughout the domain is the northwest corner of the box (stations 24 to 32). With respect to the IN seasonal variability at intermediate depths, the three concentrations do not present large differences between the values measured in fall and spring (Figs. 7 and 3). In both seasons the concentrations of SiO_2, NO_3 and PO_4 are 4-6, 2-6 and 0.2-0.4 $\mu mol\,kg^{-1}$ higher in AAIW than in MW (Tab. 2). The NADW is characterized by a moderate increase of SiO_2 and by a slight decrease of NO_3 and PO_4 with respect to the values documented here at intermediate levels. In both seasons, the maximum concentrations of SiO_2 are 28-29 $\mu mol\,kg^{-1}$. Nevertheless, and specifically in spring, maximum concentrations of NO_3 and PO_4, 28 $\mu mol\,kg^{-1}$ and 1.8-1.9 $\mu mol\,kg^{-1}$, are lower than those recorded at intermediate levels, providing a similar vertical variability as that reported by Machín et al. (2006) (Tab. 2).

DOC concentrations are higher and more widely distributed in the water column in fall than in spring, when the DOC maximum values are more confined to surface and central waters (Figs. 8 and 6, Tab. 2). This fact is especially significant in the southern transect occupied by SACW (Fig. 6). SACW presents maximum concentrations of DOC $35-40\,\mu mol\,L^{-1}$ lower than those found for NACW (Tab. 2). This difference is more pronounced in spring season (Tab. 2). In addition, the fall DOC observations present a larger variability in central waters as previously seen for IN. Lower DOC concentrations are observed for stations sampled in the western transect while the highest concentrations are recorded in the stations next to the African slope with values above $100\,\mu mol\,L^{-1}$ (Fig. 8). On the other hand, it is noteworthy the high concentrations of DOC recorded at intermediate waters of the northern transect in both cruises (Figs. 8 and 6).

4 THE INVERSE MODEL

An inverse box model is applied to the hydrographic data of the two COCA cruises to provide the absolute velocity field across the three sections (Wunsch, 1978). This method has been widely applied in different areas of the Atlantic Ocean as an efficient method to obtain absolute geostrophic flows (Martel and Wunsch, 1993; Paillet and Mercier, 1997; Ganachaud, 2003a; Machín et al., 2006; Pérez-Hernández et al., 2013; Hernández-Guerra et al., 2017; Fu et al., 2018). Assuming geostrophy and the conservation of mass and other properties in the ocean bounded by the African coast and the hydrological sections, the velocity fields are obtained allowing an adjustment of freshwater flux and Ekman transports.

4.1 Selection of layers

The closed ocean where the inverse model is applied is divided into nine layers by means of the neutral densities defined by Macdonald (1998) and modified by Ganachaud (2003a) for the North Atlantic Ocean. This distribution is then slightly modified to include two layers instead of one between 26.85 and $27.162 \, \mathrm{kg \, m^{-3}}$ by adding the isoneutral $27.035 \, \mathrm{kg \, m^{-3}}$ as others authors have done previously in this side of the NASG (Comas-Rodríguez et al., 2011; Pérez-Hernández et al., 2013). The location of the isoneutrals are represented in Figure 2. The upper five layers group the surface and central waters, the first layer until the isoneutral $26.44 \, \mathrm{kg \, m^{-3}}$ is related to surface waters while the 4 remaining layers between $26.44 \, \mathrm{kg \, m^{-3}}$ and $27.38 \, \mathrm{kg \, m^{-3}}$ do so to central waters. The intermediate waters are found in the next two layers between 27.38 and $27.82 \, \mathrm{kg \, m^{-3}}$ while the deepest two layers below $27.82 \, \mathrm{kg \, m^{-3}}$ contain the upper deep waters.

4.2 The system of equations

The inverse box model takes into account mass conservation per layer and also in the whole water column. The salinity is actually introduced as a salinity anomaly, which is also conservative within individual layers and in the whole water column (Ganachaud, 2003b). On the other hand, heat is introduced as a heat anomaly in the two deepest layers where it is also considered conservative. The salinity and heat are added as anomalies to improve the conditioning of the inverse model and get a higher rank in the system of equations by reducing the linear dependency between equations (Ganachaud, 2003b).

Therefore, the model is composed of a set of 22 equations (10 for mass conservation, 10 for salt anomaly conservation and 2 for heat anomaly conservation). Those equations are solved for 32 and 34 unknowns, comprised of 28/30 reference level velocities in fall/spring, 3 unknowns for the Ekman transport adjustments (one unknown per section), and 1 unknown for the freshwater flux. The resulting system is undetermined and a Gauss-Markov estimator is used to select a solution by adding *a priori* information. This *a priori* information consists of the uncertainties for both the unknowns (R_{xx}) and the noise of the equations (R_{nn}).

4.2.1 Uncertainties of unknowns (R_{xx})

The geostrophic velocity field is calculated in the central position between two consecutive stations. The isoneutral selected as the reference level is the deepest common γ_n for all the stations, $27.962 \, \mathrm{kg \, m^{-3}}$ (Fig. 2). Initially, the reference level is con-

sidered as a motionless level where the geostrophic velocity is taken as null before applying the inversion. The variance of the velocity in the reference level at each location is used as a measure of the *a priori* information. These variances are calculated with an annual mean velocity extracted from the daily velocity provided by GLORYS. These velocities are interpolated to the reference level depth. This reference level depth is estimated from the climatological mean depth of $27.962 \, \mathrm{kg \, m^{-3}}$ extracted from WOA13. The stations closer to the coast in the northern and southern transects have the highest variability in the velocity field.Machín et al. (2006) provide a comprehensive sensitivity analysis of the solution with respect to the a priori information in a domain just north of the one documented here. They conclude that the final mass imbalance is quite independent of both the reference level considered and also of the a priori uncertainties in the reference level velocities.

The initial Ekman transports are estimated from the wind stress for both cruises. The uncertainty associated to these Ekman transports is related to the error in their measurements and to the variability of the wind stress. A 50% uncertainty is assigned to the initial estimate of Ekman transports. The initial freshwater flux is a climatological mean of 0.0171 Sv, which is also assigned an uncertainty of 50 % as reported in similar approaches (Ganachaud, 1999; Hernández-Guerra et al., 2005; Machín et al., 2006).

Both the Ekman transports and freshwater flux with their uncertainties are added to the model in the conservation equations corresponding to the shallowest layer of the mass transport and salt anomaly and also to the conservation equations of total mass transport and total salt anomaly.

4.2.2 Uncertainties in the noise of equations (R_{nn})

The noise of each equation depends on the density field, on the layer thickness and on the uncertainties of the unknowns (Ganachaud, 1999, 2003b; Machín et al., 2006). In fact, Ganachaud (2003b) established that the largest source of uncertainty in conservation equations arises from the deviation of the baroclinic mass transport from their mean value at the time of the cruise. Thus, an analysis of the annual variability in the velocity field for the nine layers is performed. The velocity variability is examined in the mean depth between two successive isoneutral surfaces whose climatological mean depths are defined by WOA13. This variability is included in the inverse model as the *a priori* uncertainty or the noise of equations in terms of variances of mass, salt anomaly and heat anomaly transports. The velocity variance from the annual mean velocity for each layer is estimated with GLORYS and transformed into transport values by multiplying times density and the vertical area of the section involved. These *a priori* transport uncertainties are presented in Table 3. Furthermore, the uncertainty assigned to the conservation equation in the total mass is the sum of the uncertainties from the rest of the nine conservative mass equations.

The equations for salt and heat anomaly conservation depend on both the uncertainty of the mass transport and the variance of these properties (Ganachaud, 1999). In these cases, the *a priori* noise of each equation will not depend strictly on the water mass but on the layer considered, as shown in the following equation (Ganachaud, 1999; Machín, 2003):

$$R_{nn}(Cq) = a * var(C_q) * R_{nn}(mass(q)) \tag{1}$$

where $R_{nn}(Cq)$ is the uncertainty in the anomaly equation of the property (salt or heat anomaly); $var(C_q)$ is the variance of this property; a is a weighting factor of 4 in the heat anomaly, 1000 in the salt anomaly and 10^6 in the total salt anomaly; q is a given equation corresponding to a given layer.

As documented north of the Canary Islands, dianeutral velocities are of the order of 10^{-8} m s^{-1}, while dianeutral diffusion coefficients are of the order of 10^{-6} m^2 s^{-1} (Machín et al., 2006). The model results are much less affected by these values than by the reference velocities: a mean dianeutral velocity of 10^8 m s^{-1} would contribute with only 0.01 Sv, a value much less than the lateral transports obtained from the inverse model. On the other hand, the inverse model provides information only from the box boundaries and cannot be used to infer any detailed spatial distribution of dianeutral fluxes within the box. Hence, mass transports between the layers due to dianeutral transfers are considered to be negligible as compared to other sources of lateral transports and are not included in the inversion.

5   RESULTS

5.1   Velocity fields and mass transports

Figure 9 shows the reference level velocities obtained after the inversion. The variance of these velocities is also estimated by the model. The uncertainties are much higher than the values themselves and around $\pm$ (0.5-1) cm s^{-1}. During fall all non-zero values are positive, while in spring they are negative. This difference is important mainly in the western and southern transects where the module of the velocity increases reaching values of 0.3 and -0.16 cm s^{-1} in fall and spring, respectively. Furthermore, the estimated reference level velocity values in the northern transect in spring are too small, $O(10^{-4} - 10^{-5})$, while they take positive and significant values between 0.13 and 0.25 cm s^{-1} in some locations of this transect in fall.

Once the geostrophic velocities at the reference level are estimated, they are integrated into the entire water column obtaining the absolute geostrophic velocities (Fig. 10). These results are validated by comparison with the surface geostrophic velocity and the sea level anomaly, SLA, derived from altimetry during the time period that each cruise was performed (Fig. 11). To do this, the average fields of SLA and geostrophic velocity at the sea surface are calculated during each cruise and shown as a synoptic result during both surveys. Furthermore, the mass transports at the shallowest layer (red bars in Fig. 11), are superimposed with the aim of comparing these transports with the average velocity field from altimetry. A remarkable mesoscale activity can be identified at both the absolute geostrophic velocity sections (Fig. 10) and at the temporal average of SLA and the geostrophic velocity (Fig. 11). In this last case, the position of the structures at the SLA field is somewhat displaced with respect to their positions in the *in situ* velocity sections. For instance, an anticyclonic eddy is located between stations 10 and 16 in the N transect in both seasons. This eddy, observed in autumn with high velocities at intermediate layers, weakens in spring. This mesoscale structure could be part of the CEC (Sangrà et al., 2009). Furthermore, it coincides with the position of an anticyclonic eddy previously documented (Barceló-Llull et al., 2017a; Barceló-Llull et al., 2017b; Estrada-Allis et al., 2019).

In fall, two eddies are linked in the S transect, an anticyclonic one between stations 48 and 52 and a cyclonic one between stations 52 and 60, both associated with the CVFZ. In spring, two anticyclonic eddies are observed, one centred at station

36 and the other one at station 56 also associated with CVFZ. In both seasons, mesoscale structures present a large vertical extension (Fig. 10). In fall, these structures have higher velocities at IW and DW levels and they also affect a higher extension along each transect. The SLA also shows a high variability region with more intense structures in fall than in spring (Fig. 11).

290   Mesoscale structures are also visible in the vertical sections of NO_3 and PO_4 in fall, when their concentrations are higher than those observed in spring at similar locations (Fig. 7). Furthermore, high concentrations of DOC in fall at CW levels are recorded in the same area where the deep anticyclonic eddy is located, between stations 8 and 18 (Fig. 8). In spring, mesoscale structures in the vertical sections of IN and DOC at CW levels are less intense than in fall (Fig. 10). Nonetheless, DOC concentrations below the two anticyclonic structures at CW levels in spring are higher than at their surroundings.

295   The accumulated geostrophic mass transport is integrated to group the variability at different levels, having the first shallowest layer for SW, the next four layers for CW, then two layers for IW and the deepest two layers for DW (Fig. 12). The total accumulated geostrophic mass transport, integrated for all the nine layers, is also represented. The horizontal axis has the same direction as the rest of the vertical sections and the three transects are separated by two vertical dashed grey lines. Sv is used here as equivalent to $10^9 \, \mathrm{kg \, s^{-1}}$. The positive/negative transport values indicate outward/inward transports from/to the box.

300   The accumulated mass transports show a significant horizontal spatial variability, especially marked in the southern transect in accordance to the geostrophic velocity distribution (Fig. 10). The presence of significant mesoscale structures might be one of the sources for the total imbalances in the accumulated mass transport. In fall, the total imbalance is -1.43 Sv and in spring 3.55 Sv (Tab. 4).

On the other hand, the geostrophic mass transport can be integrated per layer and transect together with the total imbalance inside the box and the total mass transport uncertainty per layer (black line and horizontal black bars in Fig. 13). Moreover, Table 4 compiles these transports integrated for the different water levels, which are also represented geographically in Figure 14. More than 65% of the mass transport is given at SW and CW levels (Tab. 4). In fall, these water masses mostly get into the box across the northern and southern transects with transports of -5.61 ± 1.86 Sv and -4.35 ± 1.48 Sv, respectively; the mass leaves the box by flowing westward with a value of 5.96 ± 1.75 Sv. In spring, water masses also get in the box mostly through the northern transect with -6.69 ± 1.63 Sv but they leave along the western and southern transects with transports of 4.05 ± 1.75 Sv and 5.20 ± 1.55 Sv, respectively. It is remarkable how the inward transport in fall across the southern transect is reversed to a net outward flow in spring at the southern transect (Fig. 13).

The position of CVFZ in both seasons could partly explain that seasonal variability in the mass transports at central levels (Fig. 15). In fall, the CVFZ is located further from the African coast, so SACW is present at almost all stations of the south transect. This location of the CVFZ prevents a latitudinal mass transport from north to south. However, in spring the CVFZ is closer to the African slope allowing an important mass transport from north to south.

Between 5 and 30% of the mass transport is given in intermediate levels (Tab. 4). In fall, the intermediate water transport directs northward in the southern transect with -1.93 ± 1.69 Sv and it leaves the box with 1.94 ± 1.85 Sv and 0.48 ± 1.71 Sv across the northern and western transects, respectively. During spring, this transport weakens and changes its direction in the northern and southern transects with transports of -0.48 ± 1.65 Sv and 0.39 ± 1.73 Sv, respectively, increasing its westward transport to 1.21 ± 1.68 Sv.

The mass transport in deep water layers barely exceeds 3% (Tab. 4). An exception is the 8% given in the northern transect during fall where the estimated transport is 0.73 ± 1.71 Sv. In both cruises the transport at deep levels is nearly balanced.

5.2 Nutrient and DOC transports

325 DOC and IN transports are obtained by multiplying their concentration times mass transports. DOC, IN and geostrophic velocities are obtained at different locations, so they need to be interpolated to a common grid. In the case of DOC, the velocities are horizontally interpolated to the locations where the concentrations of DOC are taken and, in a second step, the concentrations of DOC are linearly interpolated to the depths of the geostrophic velocities. On the other hand, the *in situ* measurements of IN are scarce at IW and DW where their concentrations become higher. Therefore, instead of using the
330 observational data, the average outputs of GLORYS-BIO are used to estimate the IN transports. SiO_2, NO_3, and PO_4 mean concentrations are interpolated to the grid nodes where the geostrophic velocities are estimated by the inverse model.

DOC transports are obtained by subtracting a refractory concentration of 40 $\mu mol\,L^{-1}$ from the measured DOC (e.g., Santana-Falcón et al., 2017). This is done because the refractory fraction renewal is thousands of years, a period much longer than the time required in the processes we are focused on (Hansell, 2002). On the other hand, it should be emphasized that
335 DOC transports may be underestimated due to the scarcity of available measurements.

The IN transport values are being presented in the text always ordered as SiO_2, NO_3 and PO_4 (Figs. 16 and 17). Tables 5, 6 and 7 summarize those transports integrated per water level and transect. The errors are relative to the mass transport errors and are calculated as the standard deviations of IN transports. On the other hand, the DOC transport estimates per layer and transect are also shown in Figure 17 and summarized per water level and transect with their relative error (calculated as in the
340 IN transports) in Table 8. In order to be able to compare our transport values of IN and DOC with those reported by other authors, units of $kmol\,s^{-1}$ and $\times 10^8\,mol\,C\,day^{-1}$ are employed for IN and DOC transports, respectively, being both units equivalent.

IN enter the domain both from north and south at CW in fall. At the northern transect the transports are relatively low while at the southern one transports double the amount coming from north, with -0.41 ± 0.11, -0.78 ± 0.21 and -0.05 ± 0.01 $kmol\,s^{-1}$.
345 In spring, instead, the IN transports change their direction in the southern transect and only enter from the north with values which double those during fall, -0.40 ± 0.09, -0.90 ± 0.21, -0.06 ± 0.01 $kmol\,s^{-1}$. On the other hand, IN transports at CW layers are overall westward with low values in fall while in spring IN transports are southward and westward.

At IW levels, during fall the IN transports are inward through the southern transect with -0.27 ± 0.24, -0.36 ± 0.32, and -0.02 ± 0.02 $kmol\,s^{-1}$, and to a lesser extent through the western transect. Outward transports are observed through the north-
350 ern transect with 0.23 ± 0.22, 0.30 ± 0.28 and 0.02 ± 0.02 $kmol\,s^{-1}$. In spring, the IN enter weakly through the northern transect and leave the box crossing the western and southern transects with significant values of 0.19 ± 0.27 and 0.12 ± 0.55 $kmol\,s^{-1}$ for SiO_2; 0.25 ± 0.35 and 0.17 ± 0.75 $kmol\,s^{-1}$ for NO_3; and 0.02 ± 0.02 and 0.01 ± 0.05 $kmol\,s^{-1}$ for PO_4. In summary, while in fall the main IN transports are in the south to north direction, in spring they are mainly southwestward like the mass transport behaviour at these levels during this season (Tab. 4).

355 Finally, at DW during both seasons, the net transports of the three nutrients are similar to those at IW but with smaller values due to the low velocities at these depths, despite their high nutrient concentrations (Figs. 16 and 17). Furthermore, the relative error in these layers is always larger than the IN transport values.

In spring, DOC transports at SW and CW levels are the same order of magnitude and one order of magnitude higher than those at IW levels. In turn, these transports at IW levels are one order of magnitude higher than those at DW levels during this
360 season. In contrast, during fall at the northern transect DOC transports have the same magnitude in both SW, CW and IW and they are one order of magnitude smaller than those at CW levels during spring (Tab. 8). In this season, DOC transports at SW and CW of the western transect have unrealistic small values likely related to the low amount of measurements made in this transect during fall. DOC transports through the northern transect could also be somewhat underestimated for the same reason. However, at the southern transect during fall, the result is of the same order of magnitude as in spring.

365 In spring, DOC transports behave in a similar way in all the water column. At SW and CW levels, $-2.33\pm0.57 \times 10^8 \,\mathrm{mol\,C\,day^{-1}}$ enter through the northern transect, of which $0.89\pm0.25 \times 10^8 \,\mathrm{mol\,C\,day^{-1}}$ leave the box through the southern transect and approximately a half of it through the western transect. During fall, there is an important outward DOC transport at SW, CW and IW levels, specially southward through the southern transect at SW and CW levels with a total of $1.48\pm0.66 \times 10^8 \,\mathrm{mol\,C\,day^{-1}}$ (Tab. 8).

370 Two opposite trends can be observed when both cruises are compared. In fall the IN net transports are -0.34 ± 0.20, -0.67 ± 0.40 and $-0.04\pm0.02 \,\mathrm{kmol\,s^{-1}}$ at CW levels; -0.17 ± 1.07, -0.23 ± 1.39 and $-0.01\pm0.09 \,\mathrm{kmol\,s^{-1}}$ at IW levels, and -0.12 ± 0.25, -0.10 ± 0.21 and $-0.01\pm0.01 \,\mathrm{kmol\,s^{-1}}$ at DW levels. The amount of nutrients entering the box is larger than those leaving the box with the exception at the shallowest level where the IN leave the box (Tabs. 5, 6 and 7 and Figs. 16 and 17). On the other hand, the net DOC transports are outward for both SW, CW and IW levels with $0.10\pm0.13 \times 10^8 \,\mathrm{mol\,C\,day^{-1}}$
375 at SW level, $1.34\pm0.80 \times 10^8 \,\mathrm{mol\,C\,day^{-1}}$ at CW levels, and $0.12\pm0.72 \times 10^8 \,\mathrm{mol\,C\,day^{-1}}$ at IW (Tab. 8 and Fig. 17).

In contrast, during spring a net outward transport is obtained for the three IN with 0.28 ± 0.61, 0.57 ± 1.22 and $0.04\pm 0.08 \,\mathrm{kmol\,s^{-1}}$ at CW, 0.28 ± 0.72, 0.36 ± 0.94 and $0.02\pm0.06 \,\mathrm{kmol\,s^{-1}}$ at IW, and 0.13 ± 6.79, 0.12 ± 6.26 and $0.01\pm 0.42 \,\mathrm{kmol\,s^{-1}}$ at DW (Tabs. 5, 6 and 7, and Figs. 16 and 17). On the other hand, the DOC net transports are inward with $-0.14\pm0.08 \times 10^8 \,\mathrm{mol\,C\,day^{-1}}$ at SW level; $-0.80\pm1.72 \times 10^8 \,\mathrm{mol\,C\,day^{-1}}$ at CW levels; and $-0.01\pm0.02 \times 10^8 \,\mathrm{mol\,C\,day^{-1}}$
380 at IW levels (Tab. 8 and Fig. 17).

6 DISCUSSION

The circulation patterns in the studied area of the Canary Basin change significantly showing a temporal variability from fall to spring. The differences between the two seasons are reflected in the estimated mass transports for both cruises (Figs. 13 and 14 and Tab. 4).
385 Trade Winds are intense all year long between the Canary Islands and Cape Blanc (26° N to 21° N), and generate a quasi-permanent upwelling in this region north of Cape Blanc. In contrast, the developed EBUS intensity and its off-shore development change from fall to spring (Benazzouz et al., 2014). In the beginning of spring there is a strong heating that generates a

sharp water stratification particularly in the interior ocean of the NASG and a very intense upwelling which makes the EBUS to develop strongly far off-shore. In early fall, the EBUS weakens and becomes a shallower front which approaches towards the coast (Pelegrí and Benazzouz, 2015a). In fact, the variability related to its location and intensity may be the cause that the estimated mass transports in the north-south direction are distributed between levels of central waters and intermediate waters in fall, and that in spring these mass transports parallel to the coast are confined to the shallowest layers at central waters. On the other hand, these changes in the EBUS and in the water stratification may also be related to the westward mass transports which in fall are accentuated and confined to the levels of SW and CW, as a shallow Ekman transport, while in spring the lateral westward transport is distributed from the sea surface down to IW levels (Tab. 4 and Fig. 13).

SW transports through the N and W transects show similar patterns but in fall they are significantly more intense than in spring. In addition, CW level transports through these two transects show also similar patterns with a low variability between both seasons. The largest differences are observed in the estimated transports through the S transect which changes from fall to spring, where the transport is northward during fall and southward during spring. This observed variability in the transports in SW and CW levels in the southern part of the domain is likely related to the seasonal changes in the position of CVFZ which in turn is related to the seasonal changes in the North Atlantic Tropical Gyre (NATG), south of the domain (Pelegrí et al., 2017). The fact that the Intertropical Convergence Zone moves southward in winter and northward in summer affects the circulation patterns south and north of Cape Blanc (Lázaro et al., 2005; Stramma et al., 2008; Peña-Izquierdo et al., 2012). While in fall the CVFZ crosses the S transect in its westernmost position, in spring it moves closer to the African coast. The output of the GLORYS model matches the observations during both seasons (Fig. 15). In addition, the dynamics described by the geostrophic field of GLORYS also agree with the velocity field and the mass transports at CW levels estimated by the inverse model in the S transect for both seasons.

GLORYS velocity outputs also reproduce meso and submesoscale features associated with the CVFZ (Pérez-Rodríguez et al., 2001; Martínez-Marrero et al., 2008) which are observed directly in the S transect of the velocity sections (Fig. 10) and in the accumulative mass transport (black line in Fig. 13). Specifically during fall, the reported eddies boost a significant transport at SW and CW levels from south to north. All these results at CW levels are consistent with the late-summer and fall growth of the Mauritania Current and of the PUC and also with the decrease of the NATG currents and the weakening of the Guinea Dome in winter and spring seasons (Siedler et al., 1992; Lázaro et al., 2005; Peña-Izquierdo et al., 2012; Pelegrí and Peña-Izquierdo, 2015; Pelegrí and Benazzouz, 2015a). The estimated transports at IW also show seasonal changes between fall and spring. This region is featured by a late summer northward progression of AAIW observed in fall, and by a weak southward flow of MW in spring (Machín et al., 2010). The northward significant mass transports observed in fall at the north and south transects is consistent with the northward spreading documented for AAIW (Machín and Pelegrí, 2009; Machín et al., 2010).

In general, the estimated transport of the three IN shows similar patterns, very marked by the mass transport variability during both seasons. The level with the highest transport in all the nutrients at both seasons is the deepest CW layer. This is quite in agreement with the local maximum of remineralization found for all tracers in the upper intermediate layer Fernández-Castro et al. (2018).

CW levels are featured by a relatively high biological production and therefore a nutrient deficit, and also by large geostrophic velocities. During fall the amount of IN that enters the box through N and S transects is larger than the IN quantity that leaves the box through the W transect. In spring, on the other hand, the amount of IN transported outward through the W and S transects is larger than the IN which enters from the north.

At IW levels the concentrations of IN are high and stable related to the dominant remineralization process. During spring, the spatial distribution of the three IN transports are the same as at CW levels with smaller values. In this season the transports of IN are directed westward through the W transect towards the oligotrophic open ocean. In fall, the IN transports at IW levels have a behaviour different than at CW levels being the main transport in the south-north direction.

The most significant differences between the DOC transports in fall and spring are obtained in the first and second shallowest layers where there are high lateral velocities and where the euphotic layer is located. During fall, the DOC quantity that enters by the north transect is a third of the amount that leaves the region by the south. In the spring, however, the large amount of DOC that enters the domain from the north doubles the quantity that leaves it by the S transect while a quarter does by the western transect.

In spring, when the stratification is less marked, the most significant and deepest transports of IN are observed toward the open ocean in central and intermediate water levels. However, in fall, when the water column is more stratified and the upwelling process is the main physical forcing for nutrient supply at CW levels (Pastor et al., 2013), the IN transports toward oligotrophic interior ocean is less than in spring. In fact, while in the western transect during spring the IN transports increase with depth to their maximum values at the deepest central layer, in fall the opposite occurs, since the westward IN transports decrease with depth until cancelling at the last central layer; these transports reverse towards the coast at the two intermediate layers (green line in Figs. 16 and 17).

On the other hand, DOC transports are deeper and more intensified toward the open ocean during spring than in fall. Nonetheless, in fall there is an important and deeper transport of IN in a direction parallel to the coast. In fact, at IW DOC concentrations accumulate next to the African coast in the upwelling region. Furthermore, inside the upwelling region at the N and S transects in fall, the two observed mesoscale anticyclonic eddies could enhance this process.

The variability in intensity of the stratification, strength of upwelling and the position of the boundary between the upwelling and the oligotrophic interior ocean together with important meso and submesocale structures control the nutrients availability at CW and IW waters. It is also deduced from DOC transport estimates that the upwelling drives the changes in the size of the high production domain and equivalently, the position for the eastern boundary of the oligotrophic region in this area (Pastor et al., 2013).

The estimated transports of IN and DOC tell us that in fall there is a pronounced import of IN into the domain (with the exception of the SW layer) and a moderate export of DOC, especially at CW and IW levels. On the other hand, during spring there is a pronounced export of IN from the domain at CW and IW levels and a slight import of DOC at the shallowest CW levels and at the SW layer.

The observations used so far provide nutrient fluxes during two cruises performed only at two different seasons of the years 2002 and 2003. Thus, the full seasonal variability cannot be addressed with *in situ* observations from those years. Instead, in

this section the seasonal variability is analysed based on numerical modelling outputs, to depict the context where the *in situ* nutrient fluxes are evaluated. To do so, the time span that contains both cruises of the COCA project from the 1st of July 2002 to the 30th of June 2003 is analysed with a climatological approach: summer comprises the months from July to September, fall from October to December, winter from January to March and finally spring from April to June.

The analyses are performed at 3 different key points located in each transect during both cruises (Fig. 18). The northern point is located between stations 18 and 20, the western one between stations 36 and 38 and the southern point between stations 50 and 52. These locations are chosen as the most representative points of each transect. Nutrient profiles at each transect are analyzed for both seasons and the key points are selected where the three nutrients profiles are consistent with their average distribution. In the case of northern and southern transects, the key points are located at the intermediate point between the upwelling area and the oligotrophic open ocean, where the nutrient concentrations remain fairly stable among seasons. At the western transect, the middle position is considered to be the representative point since all nutrients profiles are markedly homogeneous along this transect and, in addition, nutrient concentrations are rather constant from fall to spring (middle column in Fig. 6).

The biogeochemical model is combined with the physical model to obtain the seasonal nutrient fluxes at the three key points (Fig. 18). Overall, nutrient fluxes are negligible at surface, where nutrients are depleted as a result of the photosynthetic activity. On the other hand, nutrient fluxes usually present their largest values in the depth range from 500 m to 1000 m, as a combination of relatively large both currents and nutrient concentrations. Nutrient fluxes at the northern point present a somewhat complex vertical structure, with opposite patterns above and below some 600 m depth. Above 600 m depth, nutrient fluxes are northward in fall, while they are southward in the rest of the seasons. Below that depth, nutrient fluxes are southward in fall, while they are northward for the remaining seasons. Once the nutrient fluxes from *in situ* observations are considered, some differences arise from both datasets. On the one hand, during spring both results indicate a southward nutrient flux above 500 m, while below that depth nutrient fluxes are southward for the *in situ* observations and northward for the numerical results. On the other hand, in fall the nutrient fluxes are southward in the entire water column for the *in situ* observations, while for the numerical results they are northward in the upper 500 m depth and southward in the remaining water column. In any case, the intensities in the nutrient fluxes from *in situ* data and from numerical modelling outputs are quite similar.

In both the western and southern points, the fluxes present a much simpler vertical structure. In the western point, nutrient fluxes in the whole water column are westward in winter and spring, while they are eastward in summer and fall. On the other hand, the maximum nutrient fluxes are obtained for winter and summer seasons, while the minimum values are estimated for the spring and fall seasons. Nutrient fluxes estimated from *in situ* observations present the same direction as those estimated by the numerical model at both seasons, though somehow the *in situ* results duplicate the numerical values. In the southern point, nutrient fluxes are southward in fall and winter, while they are mainly northward in spring and summer. It might be noteworthy the southward nutrient flux mod-elled in summer at the upper 500 m depth. Nutrient fluxes from the *in situ* observations largely coincide with the numerical results, particularly in their directions below 300 m depth. In this case, the intensity from the numerical result doubles that from the *in situ* observation in spring, while roughly the opposite occurs in fall.

7 CONCLUSIONS

An inverse box model has been applied in the eastern North Atlantic to estimate mass, nutrient and organic matter transports during spring and fall seasons. The currents estimated are largely affected by mesoscale features related to the Canary Eddy Corridor and to the Cape Verde Frontal Zone. The net mass transport at SW+CW levels coincides in both seasons in the N transect with a southward flow of 5.61 ± 1.86 Sv in fall that increases in spring to 6.69 ± 1.63 Sv. In the W transect the net westward mass transport at SW+CW levels weakens from a value of 5.96 ± 1.75 Sv in fall to 4.05 ± 1.75 Sv in spring. The most remarkable change in the net mass transport at SW+CW layers occurs in the southern transect where in fall the net mass transport is northward with a value of 4.35 ± 1.48 Sv, while in spring it is southward with a value of 5.20 ± 1.55 Sv.

At IW layers, the net transport in the south-north direction is intense and northward in fall, 1.94 ± 1.85 Sv, while it weakens and reverses southward in spring, 0.48 ± 1.65 Sv. In the W transect, the net westward mass transport at IW layers is less intense in fall, 0.48 ± 1.71 Sv, than spring, 1.21 ± 1.68 Sv. Finally, the net mass transport at DW levels is small as compared to the other water levels, with the exception of the 0.73 ± 1.71 Sv estimated in the N transect during fall.

This geographical distribution of the mass transports is consistent with a south-westward flow mainly fed by the Canary Current. On the other hand, the temporal variability of mass transports in the southern section is likely related to a zonal shift of the CVFZ, which might be located in its westernmost position in fall, bolstering the presence of waters from the South Atlantic in the domain considered. At intermediate levels it must be highlighted the significant northward transport observed at both the north and south transects during fall.

With regards to the IN and DOC net transports, in fall the domain works as a nutrient sink with a total IN net import of 0.61 ± 1.97, 0.74 ± 2.40 and 0.05 ± 0.15 kmol s^{-1} for SiO$_2$, NO$_3$ and PO$_4$, respectively, while in spring it works as a source of nutrients with a total nutrient net export of 0.73 ± 0.91, 1.21 ± 1.51 and 0.08 ± 0.1 kmol s^{-1}. It is also observed that the net DOC outward transport is of $1.55 \pm 5.01 \times 10^8$ mol C day^{-1} in fall when the domain acts as a source of DOC while the net inward value of $0.95 \pm 1.19 \times 10^8$ mol C day^{-1} describes it as a DOC sink in spring.

With respect to the lateral transports of both IN and DOC to the open ocean through the W transect, during spring there is a continuous westward IN transport, 0.75 ± 0.37, 1.34 ± 0.66 and 0.08 ± 0.04 kmol s^{-1} of SiO$_2$, NO$_3$ and PO$_4$, respectively, in all the water column. These transports coincide with an important westward transport of DOC, $0.52 \pm 0.25 \times 10^8$ mol C day^{-1}, mainly at SW and CW levels. In fall, these transports weaken at CW and reverse at IW, which means that the net westward transport of IN is smaller than in spring, with values of 0.03 ± 0.01, 0.35 ± 0.13 and 0.02 ± 0.01 kmol s^{-1} for SiO$_2$, NO$_3$ and PO$_4$. Westward transport of DOC during fall are lower than in spring, with only $0.06 \pm 0.02 \times 10^8$ mol C day^{-1}.

Overall, nutrient fluxes estimated with *in situ* observation compare well with those estimated from numerical modelling outputs. The main differences in their directions are obtained in the northern section, while the differences at the western and southern sections are mainly related to their intensity.

It is still necessary to continue with the understanding of the physical and biogeochemical processes and the interactions between the productive EBUS and the interior ocean in its vicinity, especially in dynamically complex regions as this area where

the EBUS interacts with both the CVFZ and mesoscale features. Larger and more robust hydrological and biogeochemical databases would help to achieve this goal.

Acknowledgements. This work has been done thanks to the project COCA (REN2000-U471-CO2-02-MAR) and it was supported by the project FLUXES (CTM2015-69392-C3-3-R), both of them funded by the Spanish National Research Program and the European Regional Development Fund (MINECO/FEDER). Currently, NB is working on her Ph.D. with a fellowship funded by the Spanish Ministry of Economy and Competitiveness.

References

Alonso-González, I. J., Arístegui, J., Vilas, J. C., and Hernández-Guerra, A.: Lateral POC transport and consumption in surface and deep waters of the Canary Current region: A box model study, Global Biogeochemical Cycles, 23, 1–12, https://doi.org/10.1029/2008GB003185, 2009.

Álvarez, M. and Álvarez-Salgado, X. A.: Chemical tracer transport in the eastern boundary current system of the North Atlantic, Ciencias Marinas, 35, 123–139, 2009.

Álvarez-Salgado, X. A., Arístegui, J., Barton, E. D., and Hansell, D. A.: Contribution of upwelling filaments to offshore carbon export in the subtropical Northeast Atlantic Ocean, Limnology and Oceanography, 52, 1287–1292, https://doi.org/10.4319/lo.2007.52.3.1287, 2007.

Arístegui, J., Sangrá, P., Hernández-León, S., Cantón, M., Hernández-Guerra, A., and Kerling, J.: Island-induced eddies in the Canary Islands, Deep Sea Research Part I: Oceanographic Research Papers, 41, 1509–1525, 1994.

Arístegui, J., Barton, E. D., Álvarez-Salgado, X. A., Santos, A. M. P., Figueiras, F. G., Kifani, S., Hernández-León, S., Mason, E., Machú, E., and Demarcq, H.: Sub-regional ecosystem variability in the Canary Current upwelling, Progress in Oceanography, 83, 33–48, 2009.

Azam, F.: Microbial control of oceanic carbon flux: the plot thickens, Science, 280, 694–696, 1998.

Barceló-Llull, B., Sangrà, P., Pallàs-Sanz, E., Barton, E. D., Estrada-Allis, S. N., Martínez-Marrero, A., Aguiar-González, B., Grisolía, D., Gordo, C., Rodríguez-Santana, Á., et al.: Anatomy of a subtropical intrathermocline eddy, Deep Sea Research Part I: Oceanographic Research Papers, 124, 126–139, 2017a.

Barceló-Llull, B., Pallàs-Sanz, E., Sangrà, P., Martínez-Marrero, A., Estrada-Allis, S. N., and Arístegui, J.: Ageostrophic Secondary Circulation in a Subtropical Intrathermocline Eddy, Journal of Physical Oceanography, 47, 1107–1123, https://doi.org/10.1175/JPO-D-16-0235.1, http://journals.ametsoc.org/doi/10.1175/JPO-D-16-0235.1, 2017b.

Barton, E.: The poleward undercurrent on the eastern boundary of the subtropical North Atlantic, Springer, 1989.

Barton, E. D., Arístegui, J., Tett, P., Canton, M., García-Braun, J., Hernández-León, S., Nykjaer, L., Almeida, C., Almunia, J., Ballesteros, S., Basterretxea, G., Escanez, J., García-Weill, L., Hernández-Guerra, A., López-Laatzen, F., Molina, R., Montero, M. F., Navarro-Peréz, E., Rodríguez, J. M., Van Lenning, K., Vélez, H., and Wild, K.: The transition zone of the Canary Current upwelling region, Progress in Oceanography, 41, 455–504, https://doi.org/10.1016/S0079-6611(98)00023-8, 1998.

Benazzouz, A., Pelegrí, J. L., Demarcq, H., Machín, F., Mason, E., Orbi, A., Peña-Izquierdo, J., and Soumia, M.: On the temporal memory of coastal upwelling off NW Africa, Journal of Geophysical Research C: Oceans, 119, 6356–6380, https://doi.org/10.1002/2013JC009559, 2014.

Candela, J.: Chapter 5.7 Mediterranean water and global circulation, in: International Geophysics, vol. 77, pp. 419–429, Elsevier, 2001.

Comas-Rodríguez, I., Hernández-Guerra, A., Fraile-Nuez, E., Martínez-Marrero, A., Benítez-Barrios, V. M., Pérez-Hernández, M., and Vélez-Belchí, P.: The Azores Current System from a meridional section at 24.5 W, Journal of Geophysical Research: Oceans, 116, 2011.

Copin-Montegut, C. and Copin-Montegut, G.: Stoichiometry of carbon, nitrogen, and phosphorus in marine particulate matter, Deep Sea Research Part A. Oceanographic Research Papers, 30, 31–46, 1983.

Del Giorgio, P. A. and Duarte, C. M.: Respiration in the open ocean, Nature, 420, 379, 2002.

Ekman, V. W.: Über Horizontalzirkulation bei winderzeugten Meeresströmungen, R. Friedländer & Sohn, 1923.

Emery, W. J.: Water Types and Water Masses, Encyclopedia of Ocean Sciences: Second Edition, pp. 291–299, https://doi.org/10.1016/B978-012374473-9.00108-9, 2008.

Emery, W. J. and Meincke, J.: Global water masses: summary and review, Oceanologica Acta, 9, 383–391, 1986.

Estrada-Allis, S., Barceló-Llull, B., Pallàs-Sanz, E., Rodríguez-Santana, A., Souza, J., Mason, E., McWilliams, J., and Sangrà, P.: Vertical Velocity Dynamics and Mixing in an Anticyclone near the Canary Islands, Journal of Physical Oceanography, 49, 431–451, 2019.

Falkowski, P. G., Barber, R. T., and Smetacek, V.: Biogeochemical controls and feedbacks on ocean primary production, Science, 281, 200–206, 1998.

Fernández-Castro, B., Mouriño-Carballido, B., and Álvarez-Salgado, X. A.: Non-redfieldian mesopelagic nutrient remineralization in the eastern North Atlantic subtropical gyre, Progress in Oceanography, 171, 136–153, 2018.

Fiekas, V., Elken, J., Muller, T. J., Aitsam, A., and Zenk, W.: A view of the Canary Basin thermocline circulation in winter, Journal of Geophysical Research, 97, 12 495–12 510, https://doi.org/10.1029/92JC01095, 1992.

Fu, Y., Karstensen, J., and Brandt, P.: Atlantic Meridional Overturning Circulation at 14.5° N in 1989 and 2013 and 24.5° N in 1992 and 2015: volume, heat, and freshwater transports, Ocean Science, 14, 589–616, https://doi.org/10.5194/os-14-589-2018, https://www.ocean-sci.net/14/589/2018/, 2018.

Ganachaud, A.: Large-scale mass transports, water mass formation, and diffusivities estimated from World Ocean Circulation Experiment (WOCE) hydrographic data, Journal of Geophysical Research, 108, 3213, https://doi.org/10.1029/2002JC001565, http://doi.wiley.com/10.1029/2002JC001565, 2003a.

Ganachaud, A.: Error budget of inverse box models: The North Atlantic, Journal of Atmospheric and Oceanic Technology, 20, 1641–1655, 2003b.

Ganachaud, A. and Wunsch, C.: Large-scale ocean heat and freshwater transports during the world ocean circulation experiment, Journal of Climate, 16, 696–705, 2002.

Ganachaud, A. S.: Large Scale Oceanic Circulation and Fluxes of Freshwater, Heat, Nutrients and Oxygen, Ph.D. thesis, Massachusetts Institute of Technology and Woods Hole Oceanographic Institution, https://doi.org/10.1575/1912/4130, 1999.

García-Muñoz, M., Arístegui, J., Montero, M. F., and Barton, E. D.: Distribution and transport of organic matter along a filament-eddy system in the Canaries - NW Africa coastal transition zone region, Progress in Oceanography, 62, 115–129, https://doi.org/10.1016/j.pocean.2004.07.005, 2004.

García-Muñoz, M., Arístegui, J., Pelegrí, J. L., Antoranz, A., Ojeda, A., and Torres, M.: Exchange of carbon by an upwelling filament off Cape Ghir (NW Africa), Journal of Marine Systems, 54, 83–95, https://doi.org/10.1016/j.jmarsys.2004.07.005, 2005.

Hagen, E.: Northwest African upwelling scenario, Oceanologica Acta, 24, 113–128, https://doi.org/10.1016/S0399-1784(00)01110-5, 2001.

Halkin, D., Rossby, H. T., and Rossby, T.: Structure and Transport of the Gulf Stream at 73 N, JPhysOceanogr, 15, 1439–1452, 1985.

Hansell, D. A.: DOC in the global ocean carbon cycle, Biogeochemistry of marine dissolved organic matter, 2002.

Hansen, H. P. and Koroleff, F.: Determination of nutrients, Chapter 10, Methods of Seawater Analysis, Wiley-VCH Verlag GmbH, https://doi.org/10.1002/9783527613984, 1999.

Haynes, R., Barton, E. D., and Pilling, I.: Development, persistence, and variability of upwelling filaments off the Atlantic coast of the Iberian Peninsula, Journal of Geophysical Research, 98, 22 681, https://doi.org/10.1029/93JC02016, http://doi.wiley.com/10.1029/93JC02016, 1993.

Hempel, G.: The Canary Current:Studies of an Upwelling System, A Symposium held in Las Palmas, 11-14 April 1978, Secretariat of the International Council for the Exploration of the Sea, 180, 1982.

Hernández-Guerra, A., Arístegui, J., Cantón, M., and Nykjaer, L.: Phytoplankton pigment patterns in the Canary Islands area as determined using Coastal Zone Colour Scanner data, International Journal of Remote Sensing, 14, 1431–1437, 1993.

Hernández-Guerra, A., Fraile-Nuez, E., López-Laatzen, F., Martínez, A., Parrilla, G., and Vélez-Belchí, P.: Canary Current and North Equatorial Current from an inverse box model, Journal of Geophysical Research: Oceans, 110, 1–16, https://doi.org/10.1029/2005JC003032, 2005.

Hernández-Guerra, A., Espino-Falcón, E., Vélez-Belchí, P., Pérez-Hernández, M. D., Martínez-Marrero, A., and Cana, L.: Recirculation of the Canary Current in fall 2014, Journal of Marine Systems, 174, 25–39, https://doi.org/10.1016/j.jmarsys.2017.04.002, 2017.

Hernández-León, S., Putzeys, S., Almeida, C., Bécognée, P., Marrero-Díaz, A., Arístegui, J., and Yebra, L.: Carbon export through zooplankton active flux in the Canary Current, Journal of Marine Systems, 189, 12–21, https://doi.org/10.1016/j.jmarsys.2018.09.002, https://doi.org/10.1016/j.jmarsys.2018.09.002, 2019.

Hughes, P. and Barton, E. D.: Stratification and water mass structure in the upwelling area off northwest Africa in April/May 1969, Deep-Sea Research and Oceanographic Abstracts, 21, https://doi.org/10.1016/0011-7471(74)90046-1, 1974.

Jackett, D. R. and McDougall, T. J.: A Neutral Density Variable for the World's Oceans, Journal of Physical Oceanography, 27, 237–263, 1997.

Käse, R., Price, J., Richardson, P., and Zenk, W.: A Quasi-Synoptic Survey of the Thermocline Circulation and Water Mass Distribution Within the Canary Basin, Journal of Geophysical Research: Oceans, 91, 9739–9748, 1986.

Käse, R. H. and Siedler, G.: Meandering of the subtropical front south-east of the Azores, Nature, 300, 245–246, 1982.

Lázaro, C., Fernandes, M. J., Santos, A. M. P., and Oliveira, P.: Seasonal and interannual variability of surface circulation in the Cape Verde region from 8 years of merged T/P and ERS-2 altimeter data, Remote Sensing of Environment, 98, 45–62, https://doi.org/10.1016/j.rse.2005.06.005, 2005.

Luyten, J., Pedlosky, J., and Stommel, H.: The ventilated thermocline, Journal of Physical Oceanography, 13, 292–309, 1983.

Macdonald, A. M.: The global ocean circulation: A hydrographic estimate and regional analysis, Progress in Oceanography, 41, 281–382, https://doi.org/10.1016/S0079-6611(98)00020-2, 1998.

Machín, F.: Variabilidad espacio temporal de la Corriente de Canarias, del afloramiento costero al noroeste de África y de los intercambios atmósfera-océano de calor y agua dulce, Ph.D. thesis, Universidad de Las Palmas de Gran Canaria, 2003.

Machín, F. and Pelegrí, J. L.: Northward penetration of Antarctic intermediate water off Northwest Africa, Journal of Physical Oceanography, 39, 512–535, 2009.

Machín, F., Hernández-Guerra, A., and Pelegrí, J. L.: Mass fluxes in the Canary Basin, Progress in Oceanography, 70, 416–447, https://doi.org/10.1016/j.pocean.2006.03.019, 2006.

Machín, F., Pelegrí, J. L., Fraile-Nuez, E., Vélez-Belchí, P., López-Laatzen, F., and Hernández-Guerra, A.: Seasonal Flow Reversals of Intermediate Waters in the Canary Current System East of the Canary Islands, Journal of Physical Oceanography, 40, 1902–1909, https://doi.org/10.1175/2010JPO4320.1, http://journals.ametsoc.org/doi/abs/10.1175/2010JPO4320.1, 2010.

Martel, F. and Wunsch, C.: The North Atlantic Circulation in the Early 1980s-An Estimate from Inversion of a Finite-Difference Model, Journal of Physical Oceanography, 23, 898–924, 1993.

Martínez-Marrero, A., Rodríguez-Santana, A., Hernández-Guerra, A., Fraile-Nuez, E., López-Laatzen, F., Vélez-Belchí, P., and Parrilla, G.: Distribution of water masses and diapycnal mixing in the Cape Verde Frontal Zone, Geophysical Research Letters, 35, 0–4, https://doi.org/10.1029/2008GL033229, 2008.

MATLAB: version R2018b, The MathWorks Inc., Natick, Massachusetts, https://www.mathworks.com/products/matlab.html, 2018.

Mittelstaedt, E.: The upwelling area off Northwest Africa—A description of phenomena related to coastal upwelling, Progress in Oceanography, 12, 307–331, 1983.

Mittelstaedt, E.: The ocean boundary along the northwest African coast: Circulation and oceanographic properties at the sea surface, Progress in Oceanography, 26, 307–355, https://doi.org/https://doi.org/10.1016/0079-6611(91)90011-A, 1991.

Paillet, J. and Mercier, H.: An inverse model of the eastern North Atlantic general circulation and thermocline ventilation, Deep-Sea Research Part I: Oceanographic Research Papers, 44, 1293–1328, https://doi.org/10.1016/S0967-0637(97)00019-8, 1997.

Pastor, M. V., Pelegrí, J. L., Hernández-Guerra, A., Font, J., Salat, J., and Emelianov, M.: Water and nutrient fluxes off Northwest Africa, Continental Shelf Research, 28, 915–936, 2008.

Pastor, M. V., Palter, J. B., Pelegrí, J. L., and Dunne, J. P.: Physical drivers of interannual chlorophyll variability in the eastern subtropical North Atlantic, Journal of Geophysical Research: Oceans, 118, 3871–3886, https://doi.org/10.1002/jgrc.20254, 2013.

Pelegrí, J. L. and Benazzouz, A.: Oceanographic and biological features in the Canary Current Large Marine Ecosystem, Chapter 3.4, Coastal Upwelling off north-west Africa, IOC Technical Series, 115, 2015a.

Pelegrí, J. L. and Benazzouz, A.: Oceanographic and biological features in the Canary Current Large Marine Ecosystem, Chapter 4.1, Inorganic nutrients and dissolved oxygen in the Canary Current large marine ecosystem, IOC Technical Series, 115, 2015b.

Pelegrí, J. L. and Peña-Izquierdo, J.: Oceanographic and biological features in the Canary Current Large Marine Ecosystem, Chapter 3.3, Eastern Boundary currents off north-west Africa, IOC Technical Series, 115, 2015.

Pelegrí, J. L., Arístegui, J., Cana, L., González-Dávila, M., Hernández-Guerra, A., Hernández-León, S., Marrero-Díaz, A., Montero, M. F., Sangrà, P., and Santana-Casiano, M.: Coupling between the open ocean and the coastal upwelling region off northwest Africa: Water recirculation and offshore pumping of organic matter, Journal of Marine Systems, 54, 3–37, https://doi.org/10.1016/j.jmarsys.2004.07.003, 2005.

Pelegrí, J. L., Marrero-Díaz, A., and Ratsimandresy, A. W.: Nutrient irrigation of the North Atlantic, Progress in Oceanography, 70, 366–406, https://doi.org/10.1016/j.pocean.2006.03.018, 2006.

Pelegrí, J. L., Peña-Izquierdo, J., Machín, F., Meiners, C., and Presas-Navarro, C.: Deep-Sea Ecosystems Off Mauritania, Chapter 3, Oceanography of the Cape Verde Basin and Mauritanian Slope Waters, Springer, 2017.

Peña-Izquierdo, J., Pelegrí, J. L., Pastor, M. V., Castellanos, P., Emelianov, M., Gasser, M., Salvador, J., and Vázquez-Domínguez, E.: The continental slope current system between Cape Verde and the Canary Islands, Scientia Marina, 76, 65–78, https://doi.org/10.3989/scimar.03607.18C, 2012.

Pérez, F. F., Mintrop, L., Llinás, O., Glez-Dávila, M., Castro, C. G., Alvarez, M., Körtzinger, A., Santana-Casiano, M., Rueda, M. J., and Ríos, A. F.: Mixing analysis of nutrients, oxygen and inorganic carbon in the Canary Islands region, Journal of Marine Systems, 28, 183–201, https://doi.org/10.1016/S0924-7963(01)00003-3, 2001.

Pérez-Hernández, M. D., Hernández-Guerra, A., Fraile-Nuez, E., Comas-Rodríguez, I., Benítez-Barrios, V. M., Domínguez-Yanes, J. F., Vélez-Belchí, P., and De Armas, D.: The source of the Canary current in fall 2009, Journal of Geophysical Research: Oceans, 118, 2874–2891, https://doi.org/10.1002/jgrc.20227, 2013.

Pérez-Rodríguez, P., Pelegrí, J. L., and Marrero-Díaz, A.: Dynamical characteristics of the Cape Verde frontal zone, Scientia Marina, 65, 241–250, https://doi.org/10.3989/scimar.2001.65s1241, 2001.

Ruiz, S., Pelegrí, J., Emelianov, M., Pascual, A., and Mason, E.: Geostrophic and ageostrophic circulation of a shallow anticyclonic eddy off Cape Bojador, Journal of Geophysical Research: Oceans, 119, 1257–1270, 2014.

Sangrà, P., Auladell, M., Marrero-Díaz, A., Pelegrí, J. L., Fraile-Nuez, E., Rodríguez-Santana, A., Martín, J. M., Mason, E., and Hernández-Guerra, A.: On the nature of oceanic eddies shed by the Island of Gran Canaria, Deep-Sea Research Part I: Oceanographic Research Papers, 54, 687–709, https://doi.org/10.1016/j.dsr.2007.02.004, 2007.

680   Sangrà, P., Pascual, A., Rodríguez-Santana, Á., Machín, F., Mason, E., McWilliams, J. C., Pelegrí, J. L., Dong, C., Rubio, A., Arístegui, J., Marrero-Díaz, Á., Hernández-Guerra, A., Martínez-Marrero, A., and Auladell, M.: The Canary Eddy Corridor: A major pathway for long-lived eddies in the subtropical North Atlantic, Deep-Sea Research Part I: Oceanographic Research Papers, 56, 2100–2114, https://doi.org/10.1016/j.dsr.2009.08.008, 2009.

Santana-Falcón, Y., Álvarez-Salgado, X. A., Pérez-Hernández, M. D., Hernández-Guerra, A., Mason, E., and Arístegui, J.: Organic carbon
685   budget for the eastern boundary of the North Atlantic subtropical gyre: Major role of DOC in mesopelagic respiration, Scientific Reports, 7, 1–12, https://doi.org/10.1038/s41598-017-10974-y, 2017.

Schlitzer, Reiner: Ocean Data View, http://odv.awi.de., 2019.

Siedler, G., Zangenberg, N., and Onken, R.: Seasonal Changes in the Tropical Atlantic Circulation: Observation and Simulation of the Guinea Dome, Journal of Geophysical Research, 97, 703–715, 1992.

690   Smith, W. H. F. and Sandwell, D. T.: Global Sea Floor Topography from Satellite Altimetry and Ship Depth Soundings, Science, 277, 1956–1962, https://doi.org/10.1126/science.277.5334.1956, http://science.sciencemag.org/content/277/5334/1956, 1997.

Stramma, L.: Geostrophic transport in the warm water sphere of the eastern subtropical North Atlantic, Journal of Marine Research, 42, 537–558, https://doi.org/10.1357/002224084788506022, 1984.

Stramma, L. and Siedler, G.: Seasonal changes in the North Atlantic subtropical gyre, Journal of Geophysical Research, 93, 8111,
695   https://doi.org/10.1029/JC093iC07p08111, 1988.

Stramma, L., Brandt, P., Schafstall, J., Schott, F., Fischer, J., and Körtzinger, A.: Oxygen minimum zone in the North Atlantic south and east of the Cape Verde Islands, Journal of Geophysical Research: Oceans, 113, 1–15, https://doi.org/10.1029/2007JC004369, 2008.

Thomas, C., Cauwet, G., and Minster, J.-F.: Dissolved organic carbon in the equatorial Atlantic Ocean, Marine Chemistry, 49, 155–169, 1995.

700   Tomczak, M.: The CINECA experience, Marine Policy, 3, 59–65, https://doi.org/https://doi.org/10.1016/0308-597X(79)90040-X, 1979.

Tomczak, M. and Godfrey, J. S.: Regional oceanography, an introduction, Elsevier, 2nd edition edn., 2003.

Wunsch, C.: North Atlantic general circulation west of $50°$W determined by inverse methods, Reviews of Geophysics, 16, 583–620, 1978.

Wunsch, C.: The ocean circulation inverse problem, Cambridge University Press, Cambridge;New York;, 1996.

Zenk, W., Klein, B., and Schroder, M.: Cape Verde Frontal Zone, Deep Sea Research Part A. Oceanographic Research Papers, 38, S505–S530,
705   https://doi.org/10.1016/S0198-0149(12)80022-7, 1991.

Figures and tables
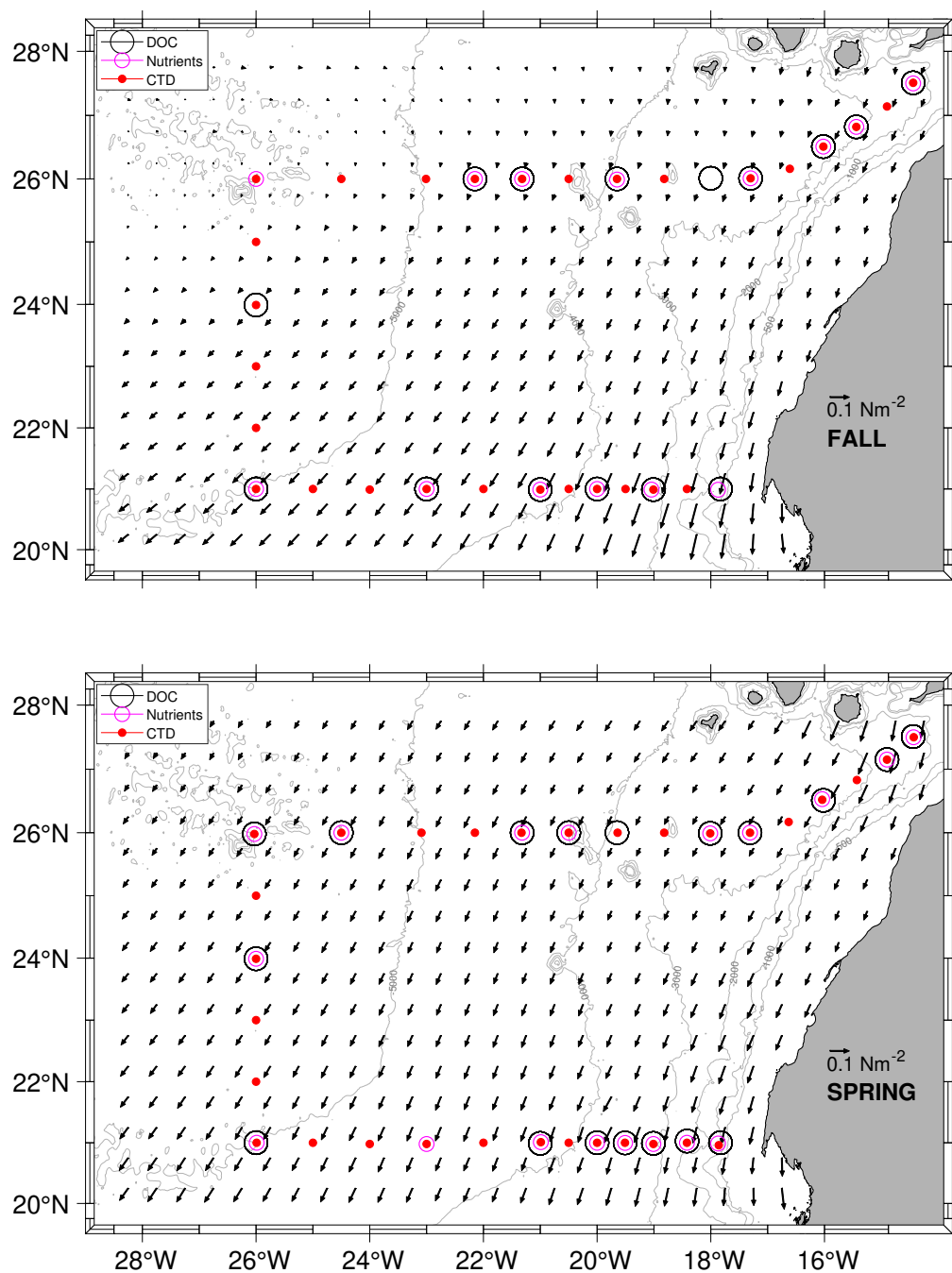
Figure 1. Hydrological (red dots), inorganic nutrients (pink circles) and DOC (black circles) sampling stations during COCA-I (top) and COCA-II (bottom) cruises. Time-averaged wind stress during each cruise is also represented with the inset arrow denoting the scale (shown with half of the original spatial resolution).
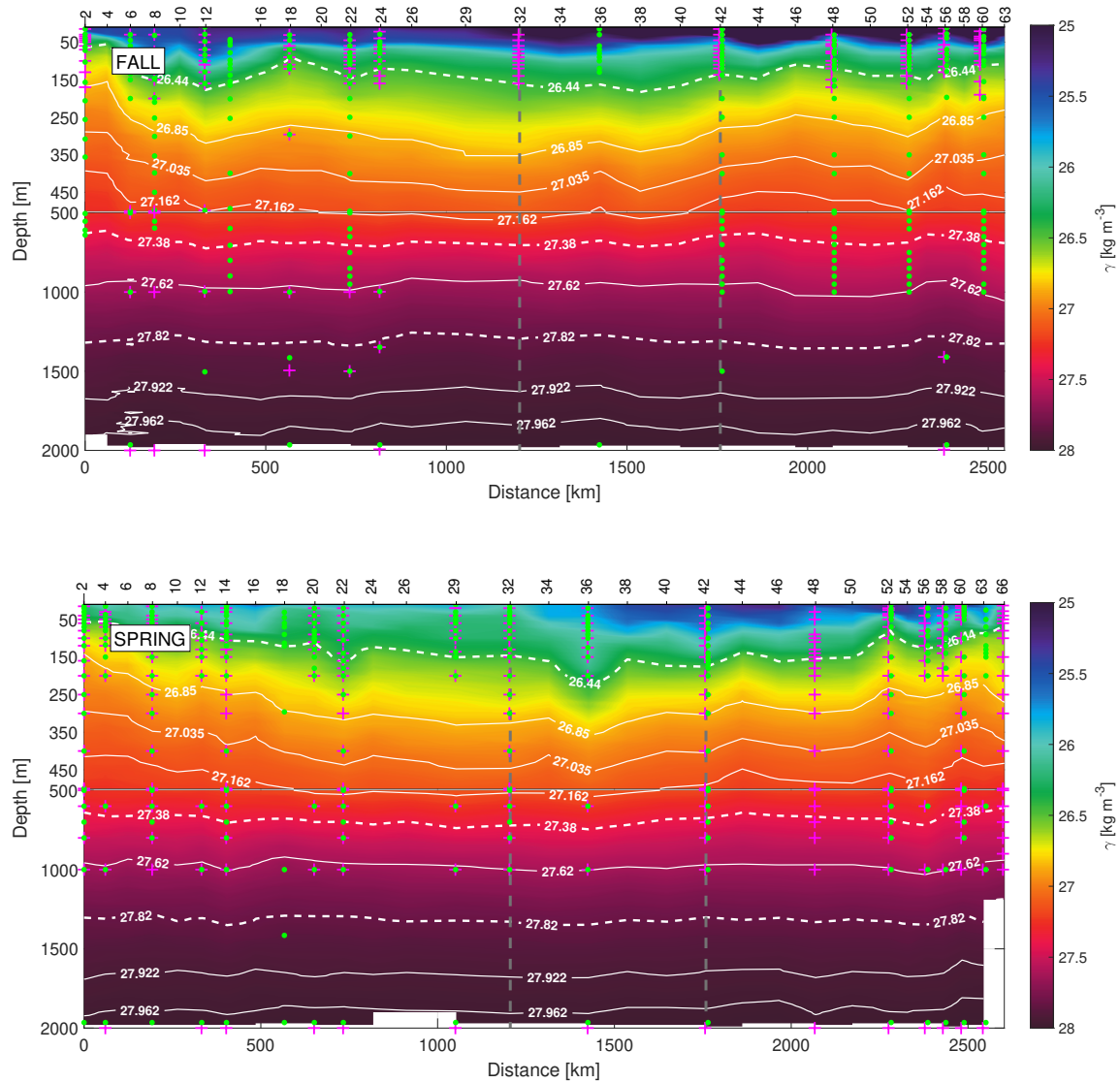
Figure 2. γ_n vertical sections during fall (top) and spring (bottom) cruises. White dashed isoneutrals limit the different water type layers. The direction chosen for the representation of the transects is the course of the vessel. Distance is calculated with respect to the first station (2). The section is divided into three transects: northern transect from east to west (from station 2 to 32), western transect from north to south (from station 32 to 42) and southern transect from west to east (from stations 42 to 63/66). The 3 transects are separated by two vertical grey dashed lines located at stations number 32 and 42. The sampling points of IN and DOC used in this work are also represented in pink crosses and green dots, respectively.
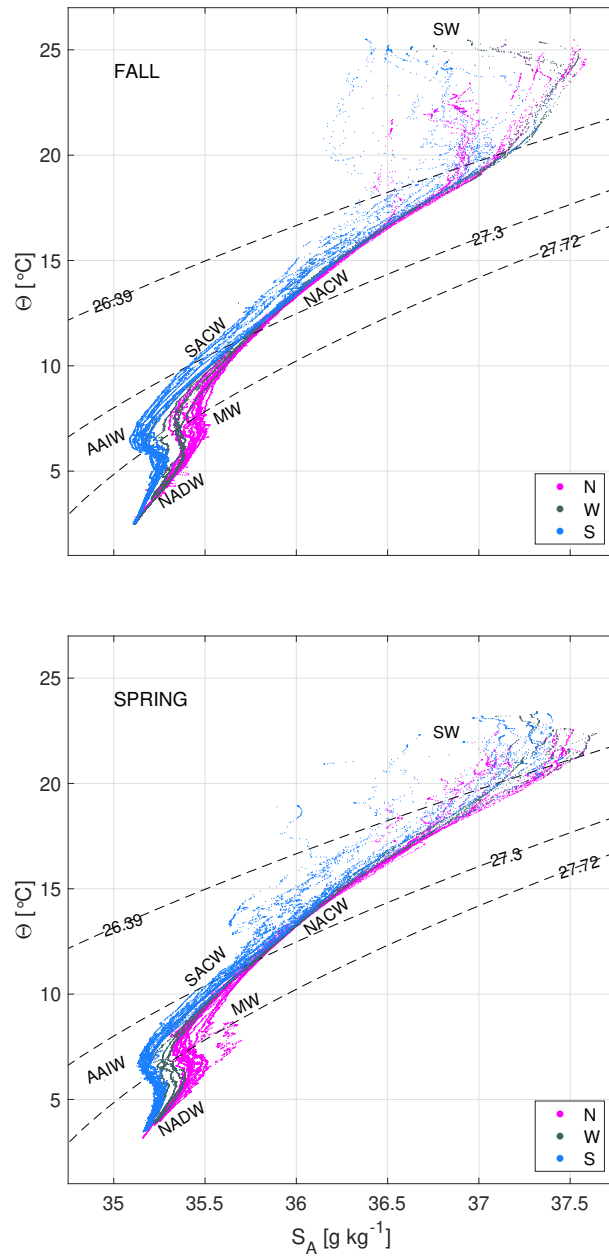
Figure 3. $\Theta - S_A$ diagrams of the hydrological measurements in fall (top) and spring (bottom) cruises. The different water masses at north (N, magenta dots), west (W, dark grey dots) and south (S, blue dots) transects are SW, NACW, SACW, AAIW, MW and NADW. Potential density anomaly contours equivalent to 26.44, 27.38 and $27.82 \, \mathrm{kg \, m^{-3}}$ isoneutrals delimit the surface, central, intermediate and deep water levels.
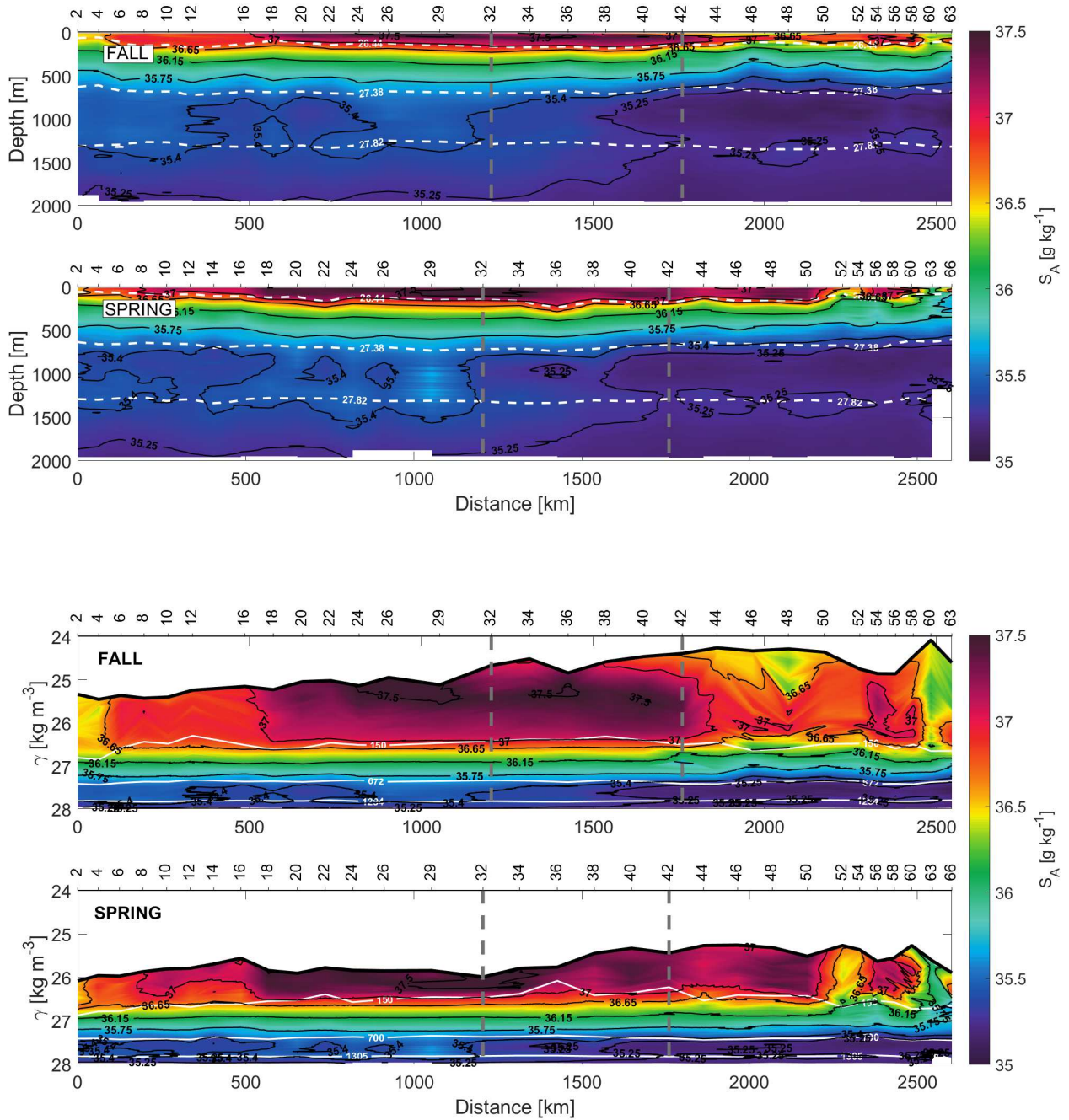
Figure 4. Sections of absolute salinity (S_A) with respect to depth (top) and γ_n (bottom) during fall and spring. In depth section (top), the isoneutrals which delimit the transports at surface, central, intermediate and deep water are represented by white dashed contours. In γ_n section (bottom), the depths of 150, 672/700 and 1294/1305 m are also shown.
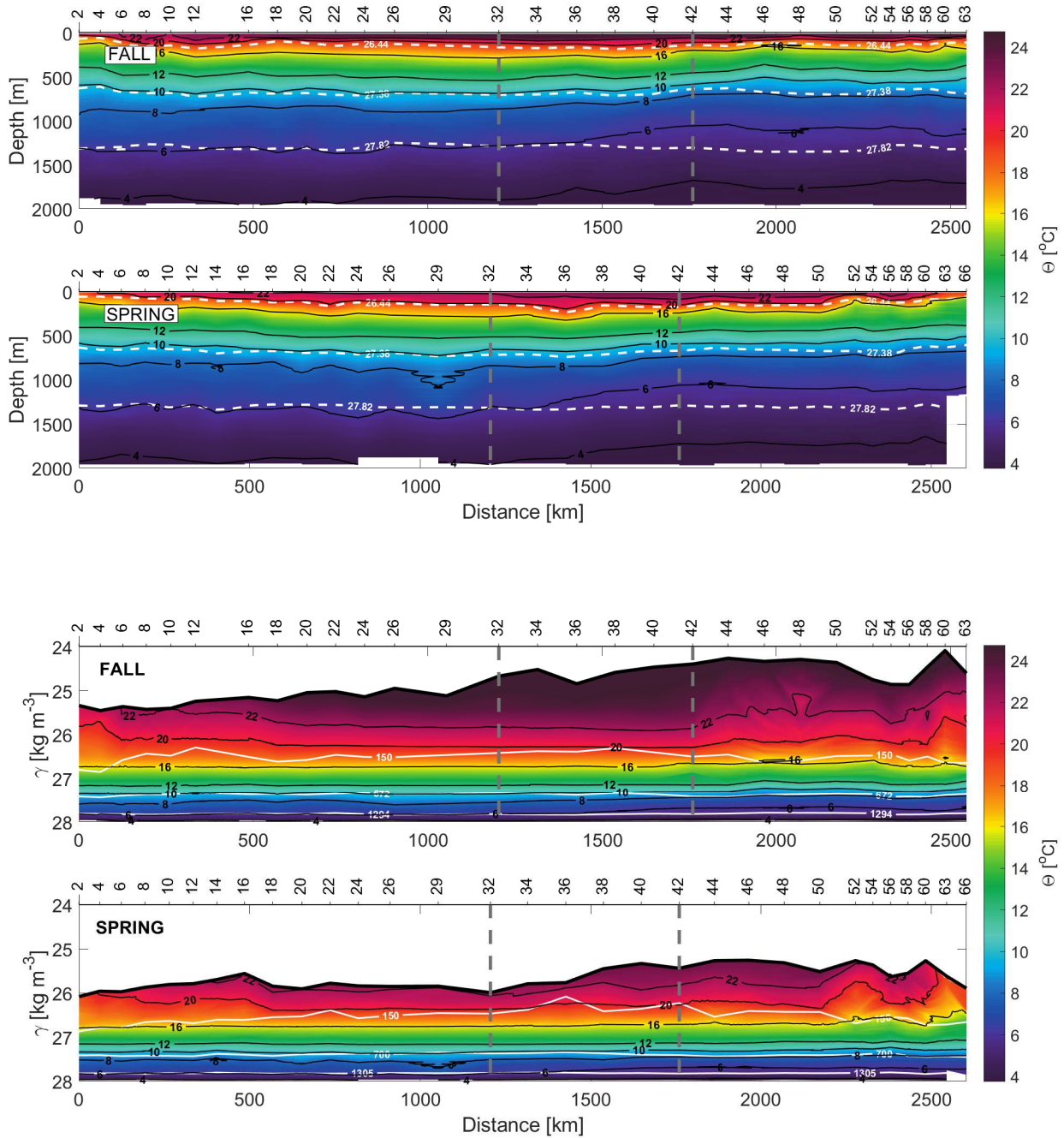
Figure 5. Sections of conservative temperature (Θ) with respect to depth (top) and γ_n (bottom) during fall and spring. In depth section (top), the isoneutrals which delimit the transports at surface, central, intermediate and deep water in the water column are represented by white dashed contours. In γ_n section (bottom), the depths of 150, 672/700 and 1294/1305 m are indicated.
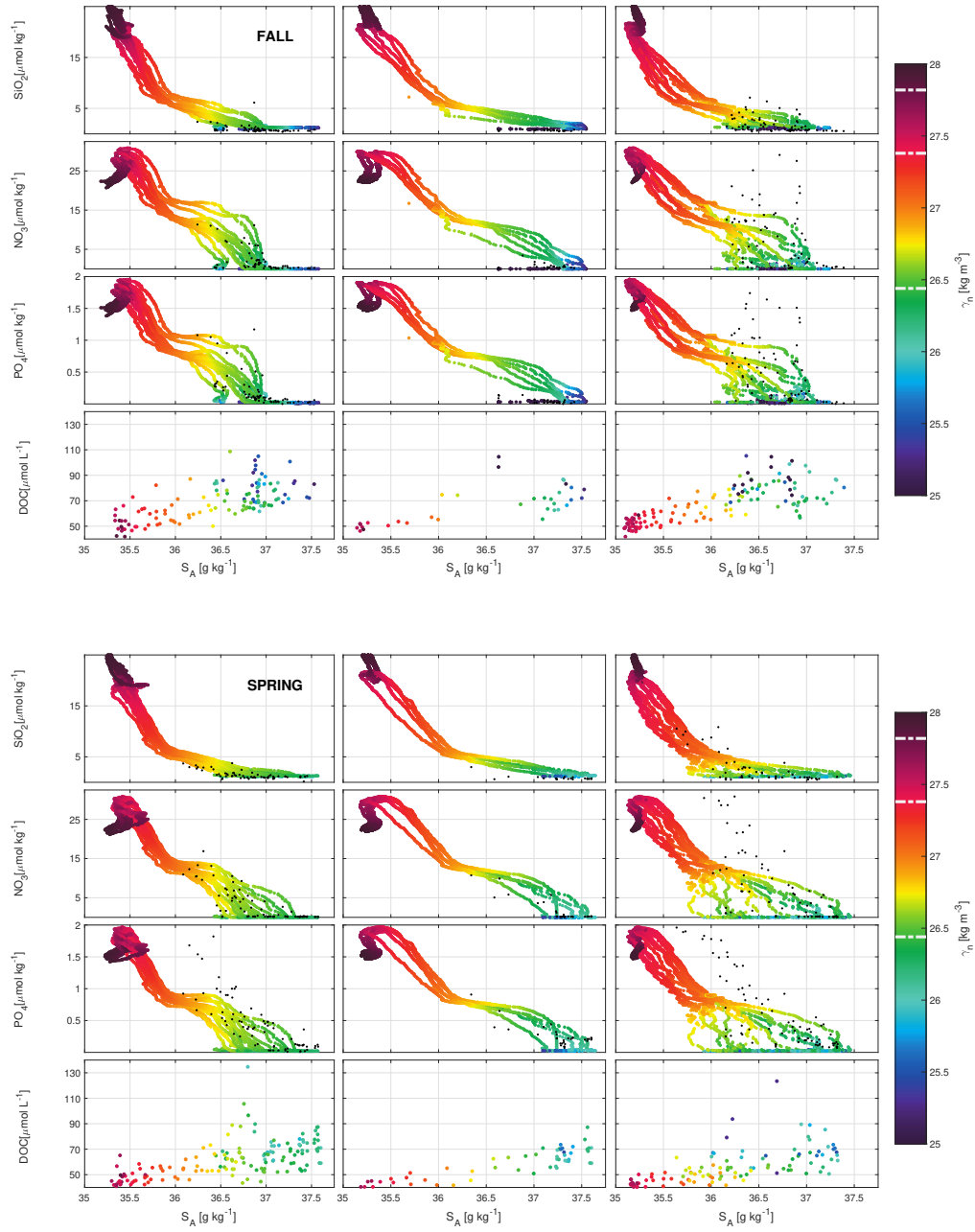
Figure 6. Scatter plots for SiO_2, NO_3 and PO_4 nutrients (µmol kg^{-1} extracted from GLORYS-BIO), and for DOC (observational data in µmol L^{-1}) with respect to S_A and γ_n at the north (left), west (middle) and south transects (right) in fall (top) and spring (bottom). The isoneutrals 26.44, 27.38 and 27.82 kg m^{-3} that limit the waters layers are indicated with white dashed lines in the colorbar. The measured IN concentrations (µmol kg^{-1}) for SiO_2, NO_X and PO_4 until 250 m depth are included as black dots.
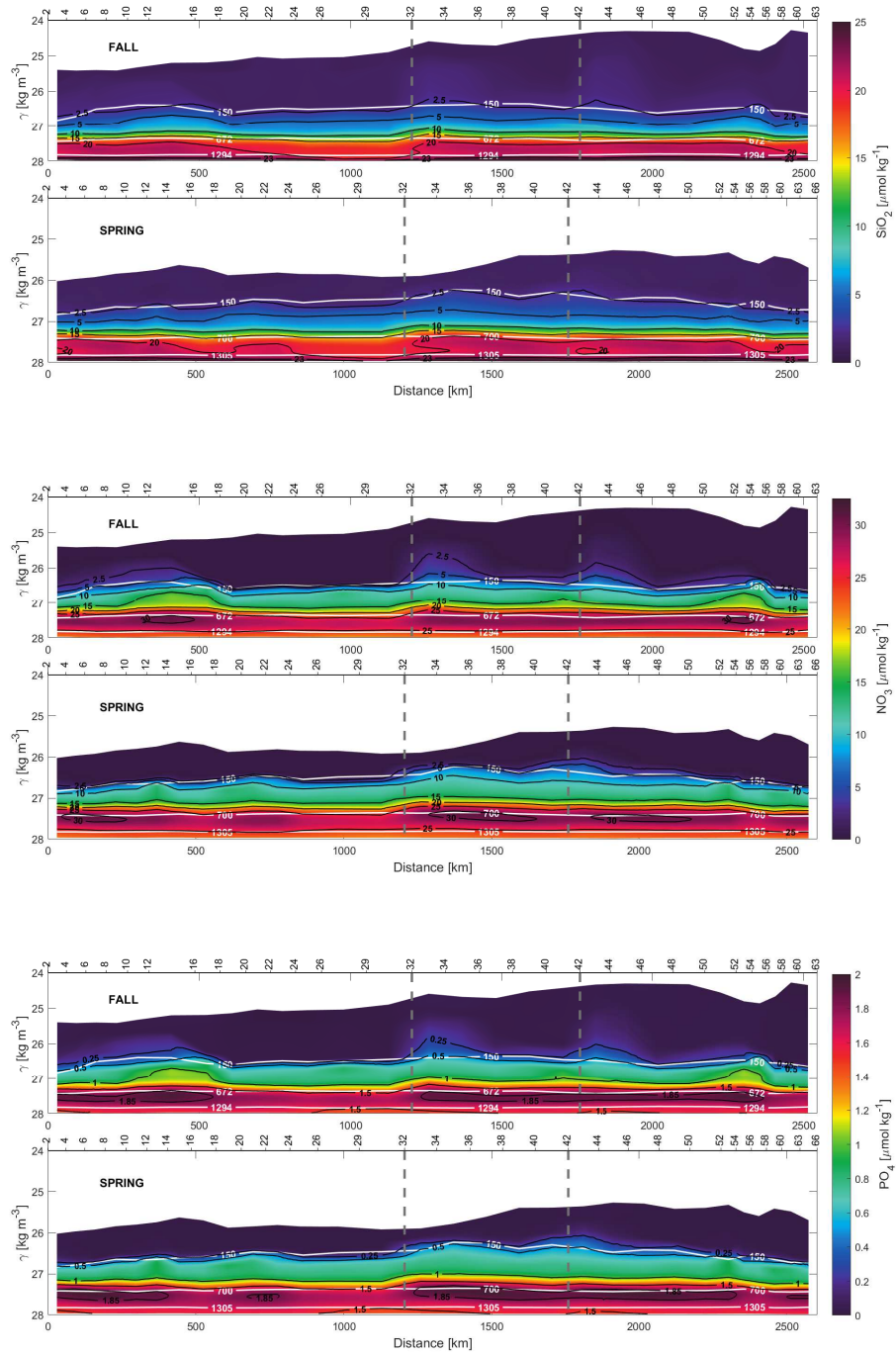
Figure 7. Sections for SiO_2 (top), NO_3 (middle) and PO_4 (bottom) concentrations with respect to γ_n during fall (top) and spring (bottom) extracted from GLORYS-BIO. The white isolines as in the γ_n sections of Figs. 4 and 5.
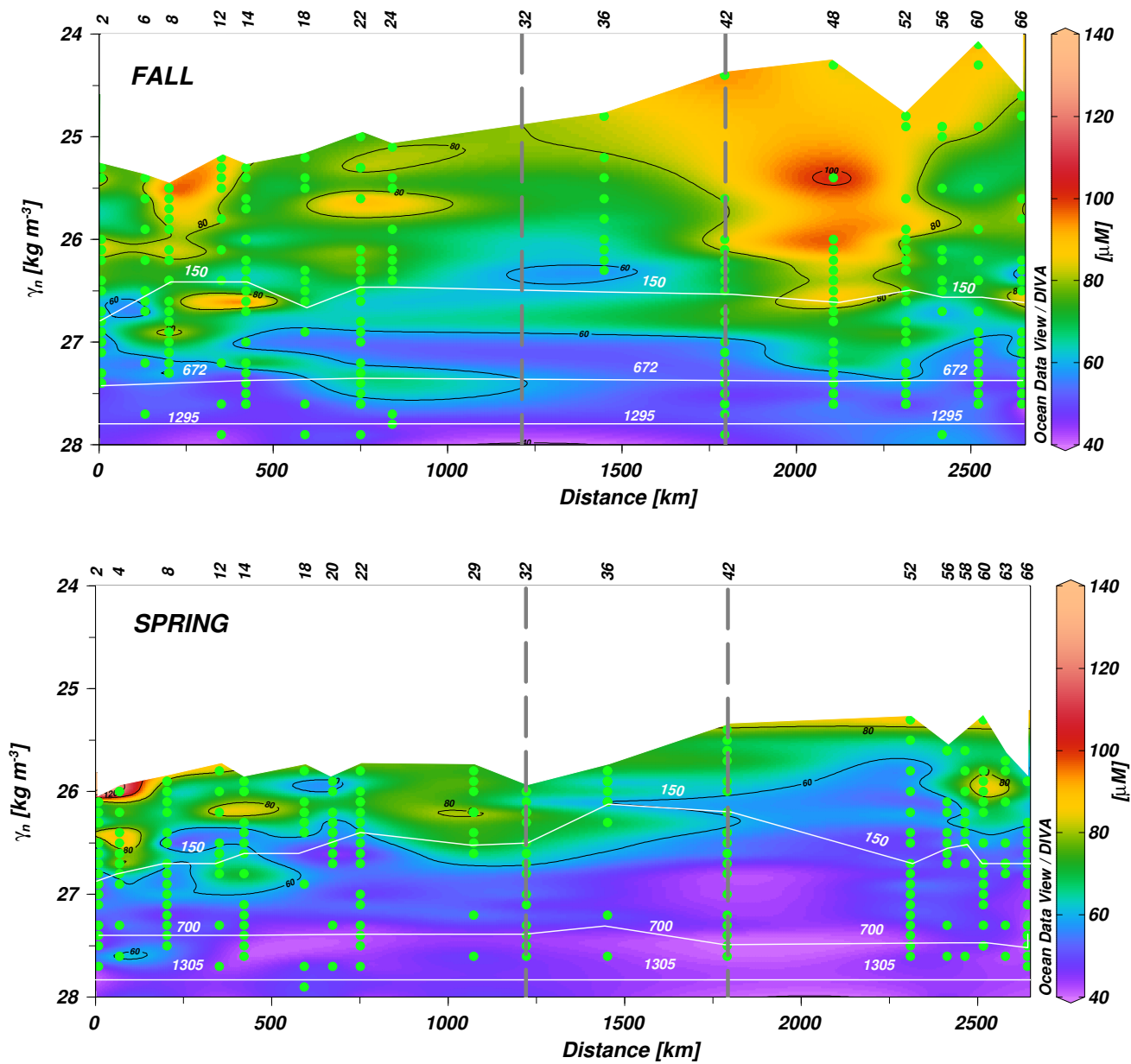
Figure 8. Sections of DOC concentration with respect to γ_n during fall (top) and spring (bottom) cruises with the white isolines as in the γ_n sections of Figs. 4 and 5.
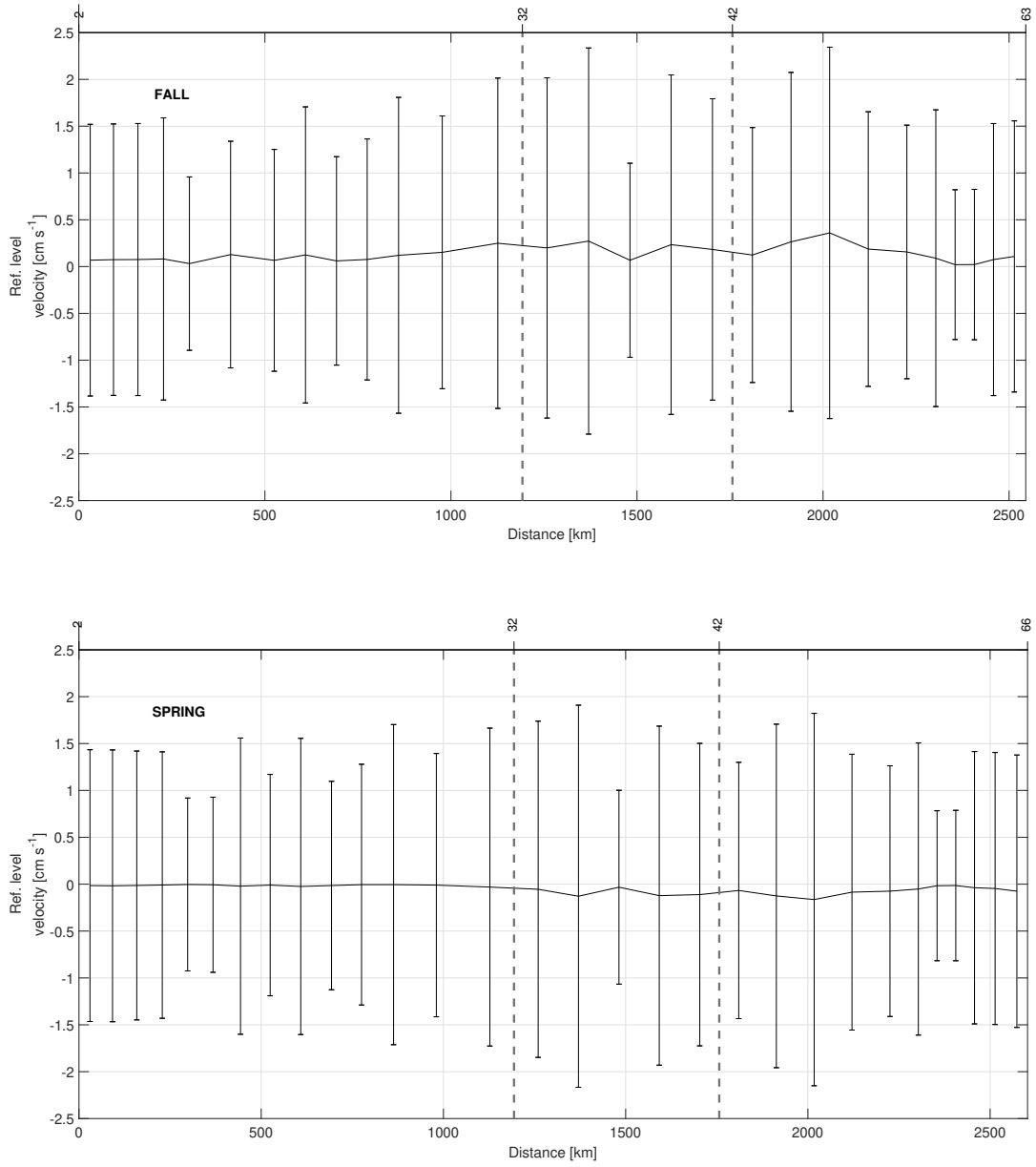
Figure 9. Reference level velocity at $27.962\,\mathrm{kg\,m^{-3}}$ and its standard deviation estimated by the inverse model during fall (top) and spring (bottom). The direction chosen for the representation is the same as in Fig. 2. The signs of the velocity are according to the geographical criterion, i.e., the velocities are positive/negative toward north/south, in the northern and southern transects and they are positive/negative toward east/west in the western transect.
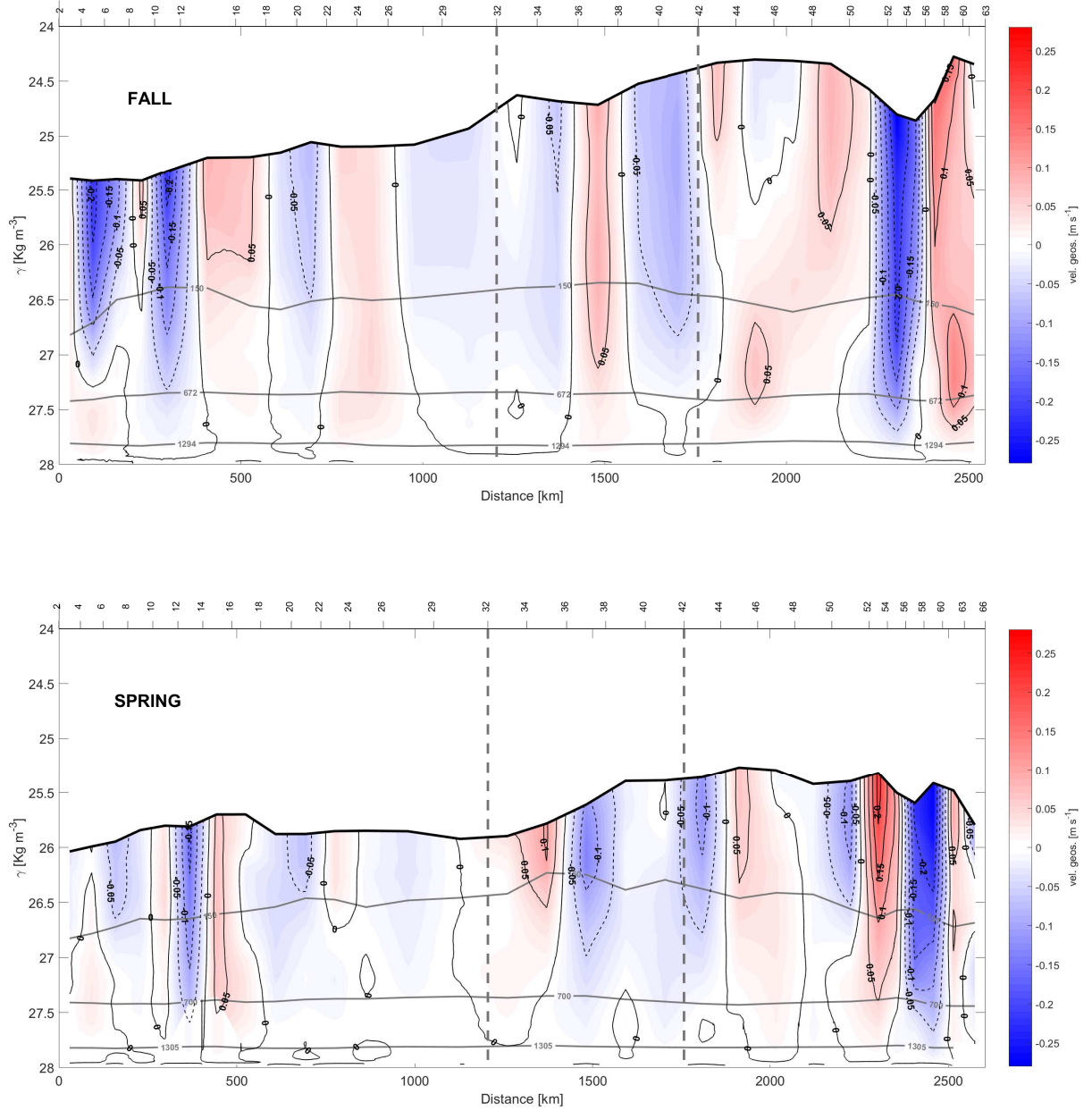
Figure 10. Sections of the absolute geostrophic velocity with respect to γ_n during fall (top) and spring (bottom). The horizontal axis has the same direction as Fig. 2 and the criterion of the velocity signs is as in Fig. 9. The depths 150, 672/700 and 1294/1305 m are highlighted by grey isolines as in the γ_n sections of Figs. 4 and 5.
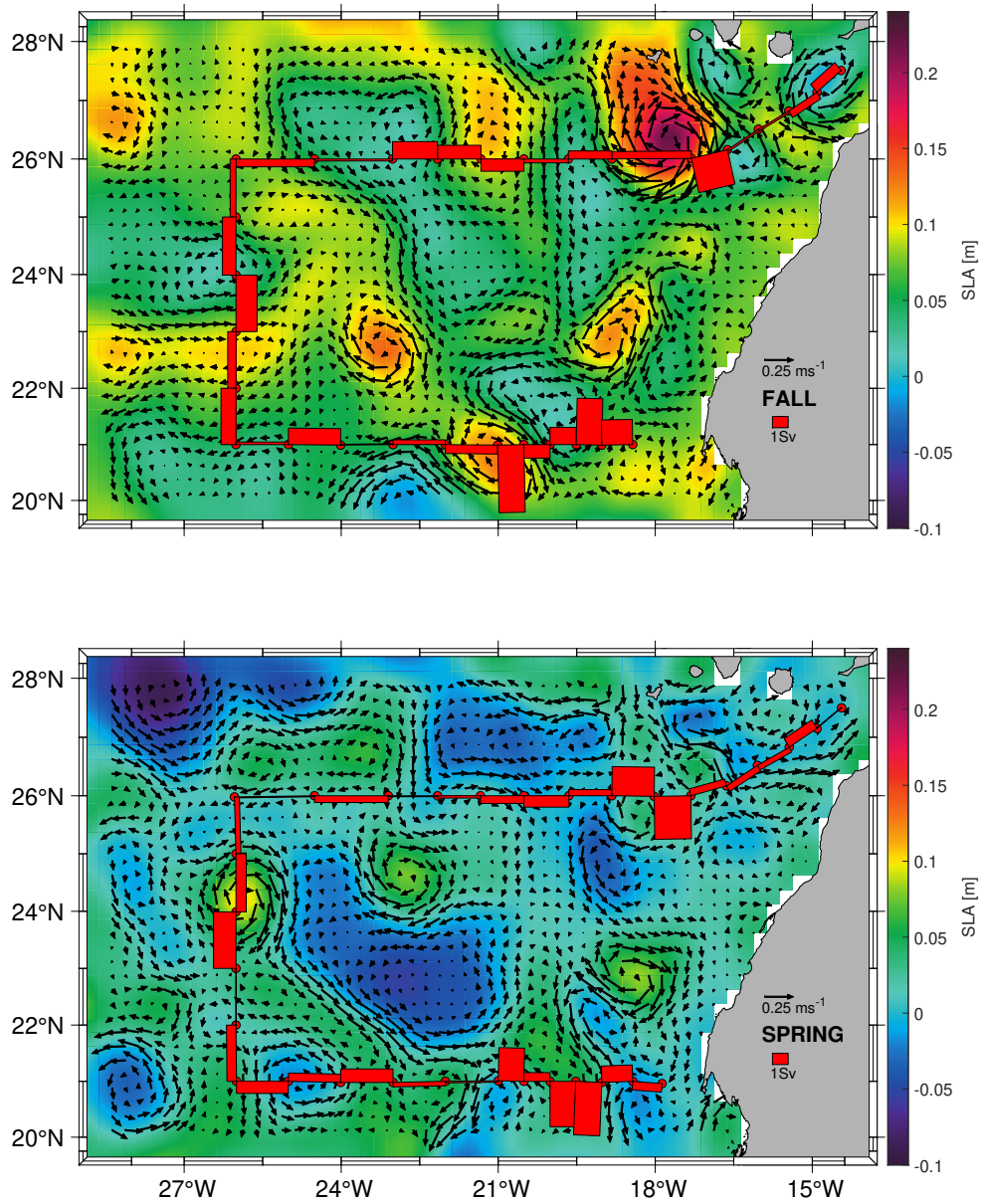
Figure 11. Average derived geostrophic velocity and SLA during fall (top), in the course of the fist cruise, and spring (bottom), in the course of the second cruise, extracted from AVISO+. The red bars represent the mass transports in the shallowest layer as estimated by the inverse model.
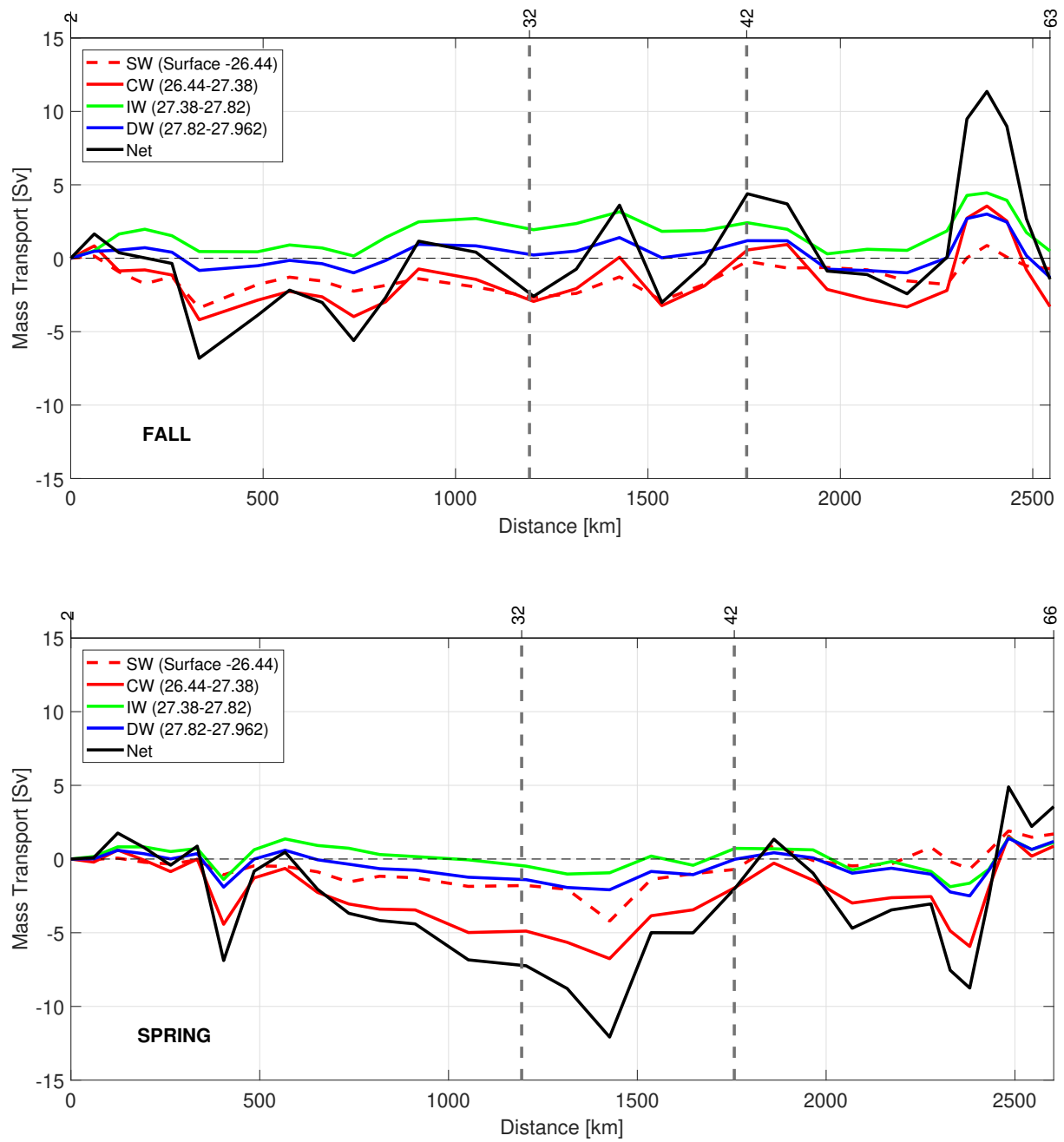
Figure 12. Accumulated mass transport along the fall (top) and spring (bottom) cruises at surface waters (SW, in red and dashed line), central waters (CW, in red line), intermediate waters (IW, in green line) and deep waters (DW, in blue line). The accumulated mass transport integrated for all the nine layers is also represented. The horizontal axis has the same direction as Fig. 2. Negative/positive values of transports along the three transects indicate inward/outward transports of box delimited by the three transects and the African coast.
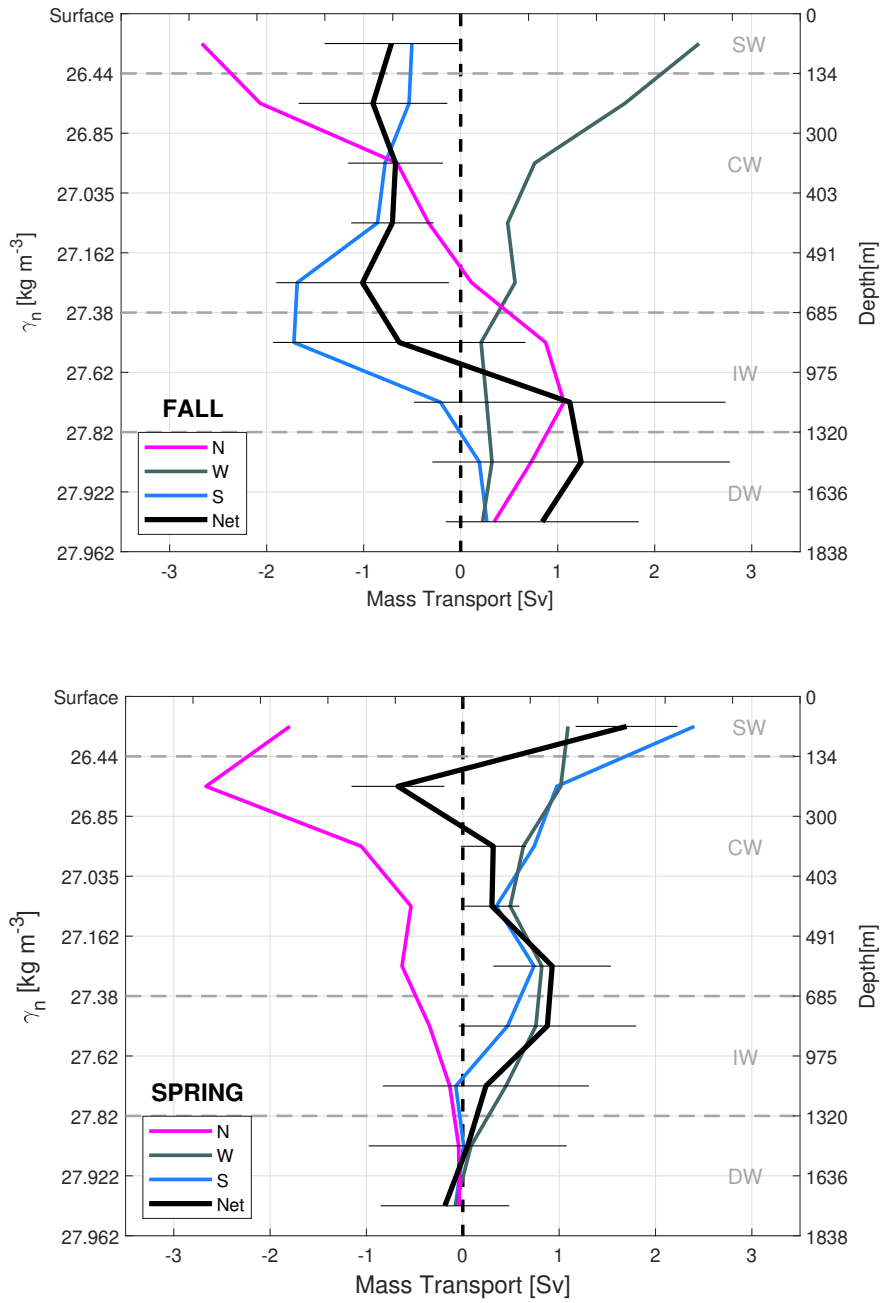
Figure 13. Accumulated mass transports per transect at north (N, magenta line), west (W, dark grey line) and south (S, blue line) transects during fall (top) and spring (bottom). See Tab. 2 to check γ_n values bounding every water layer. Negative/positive values indicate inward/outward transports as in Fig. 12. Mass conservation in the whole domain is shown by the black line. The horizontal bars represent the uncertainties estimated by the model.
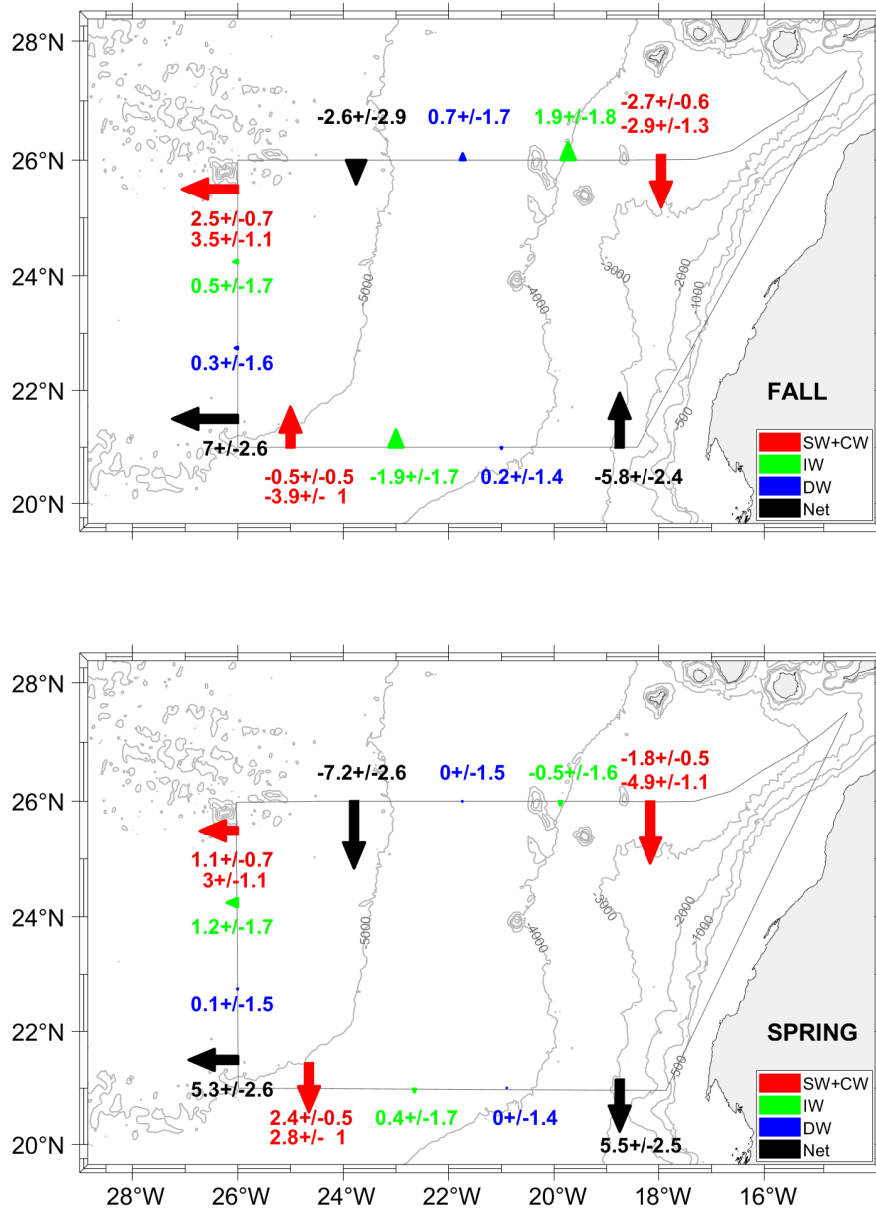
Figure 14. Mass transports with their errors (Sv) at surface and central waters (SW+CW, red arrow), intermediate waters (IW, green arrow) and deep waters (DW, blue arrow) across every transect during fall (top) and spring (bottom). Negative/positive values indicate inward/outward transports as in Fig. 12. The arrows in each transect are located in positions which optimize their visibility, representing the integrated transports along each transect. The values of transports at SW (dark red) are given next to the integrated values of transports at CW levels (in red). The red arrows represent the integrated transports for SW plus CW layers.
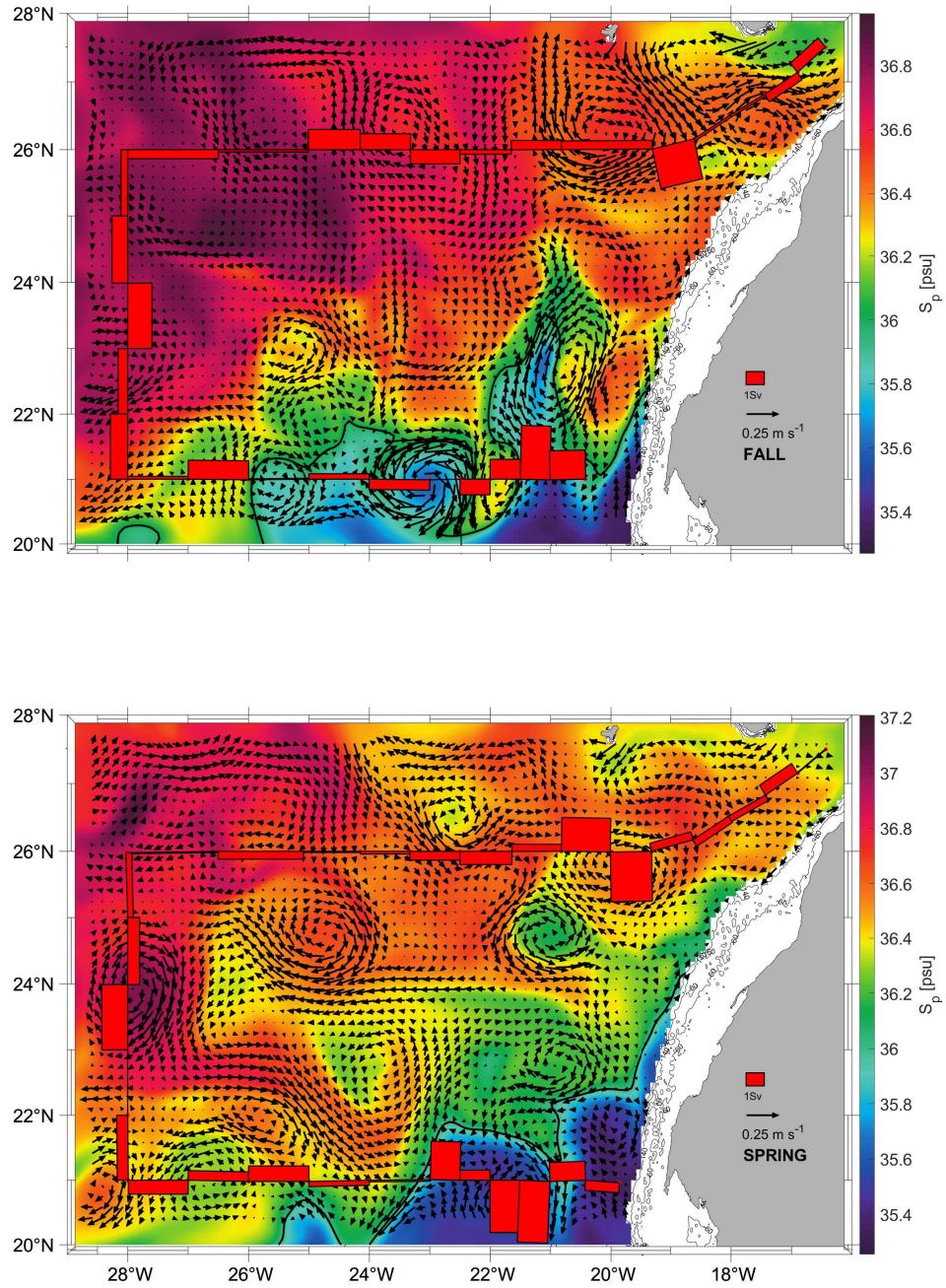
Figure 15. Mean salinity and mean geostrophic velocity at 156 m extracted from GLORYS during fall (top) and spring (bottom). The black line indicates the position of the isohaline of 36 at this depth, used to identify the CVFZ. The red bars represent mass transports in the shallowest layer as estimated by the inverse model.
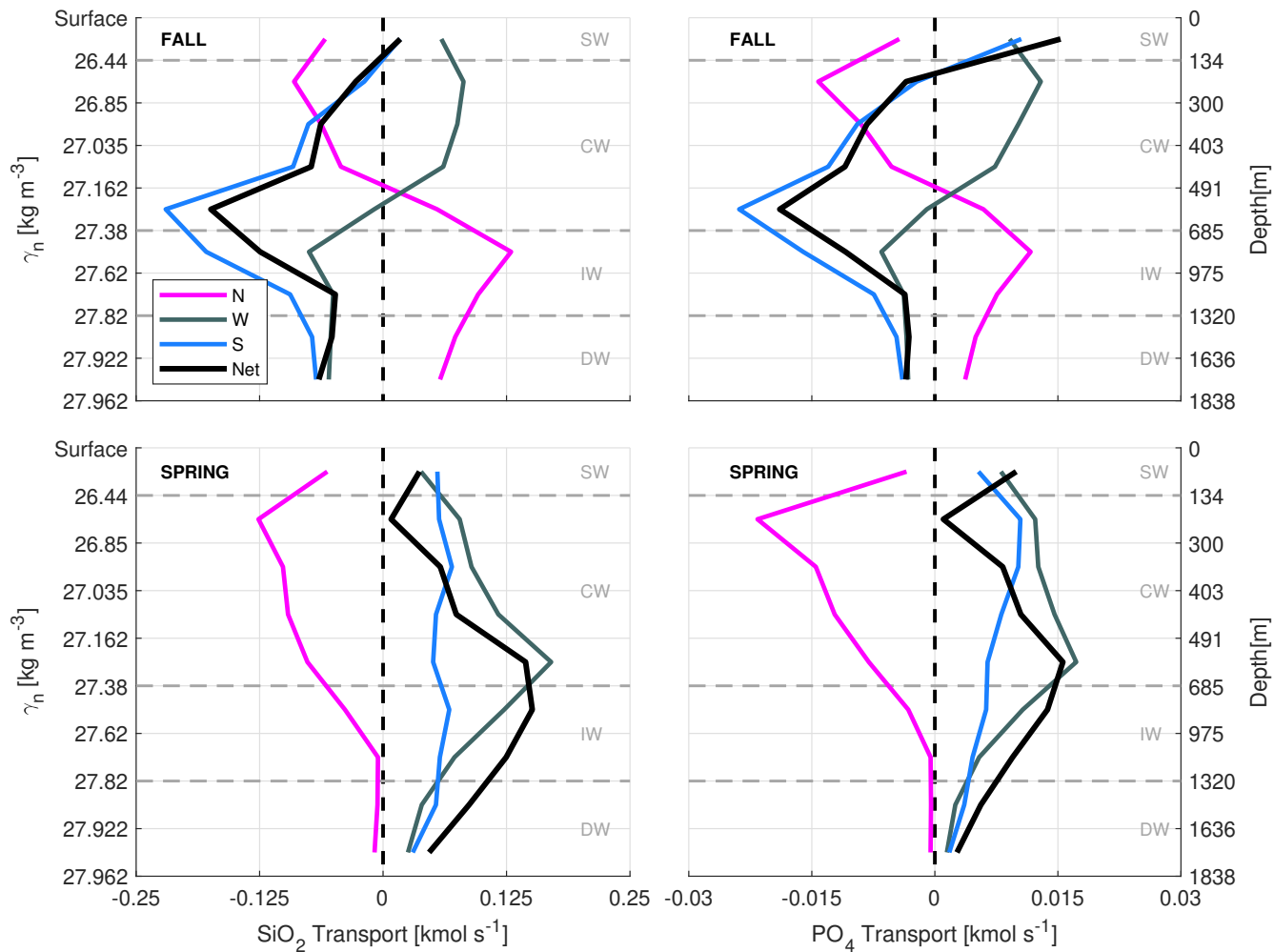
Figure 16. Accumulated SiO_2 and PO_4 transports ($\mathrm{kmol\,s^{-1}}$) at transects north (N, magenta line), west (W, dark grey line) and south (S, blue line) during fall (top) and spring (bottom). See Tab. 2 to check γ_n values bounding every water layer. Negative/positive values indicate inward/outward transports as in Fig. 12. The net transport in the whole box is shown by the black line.
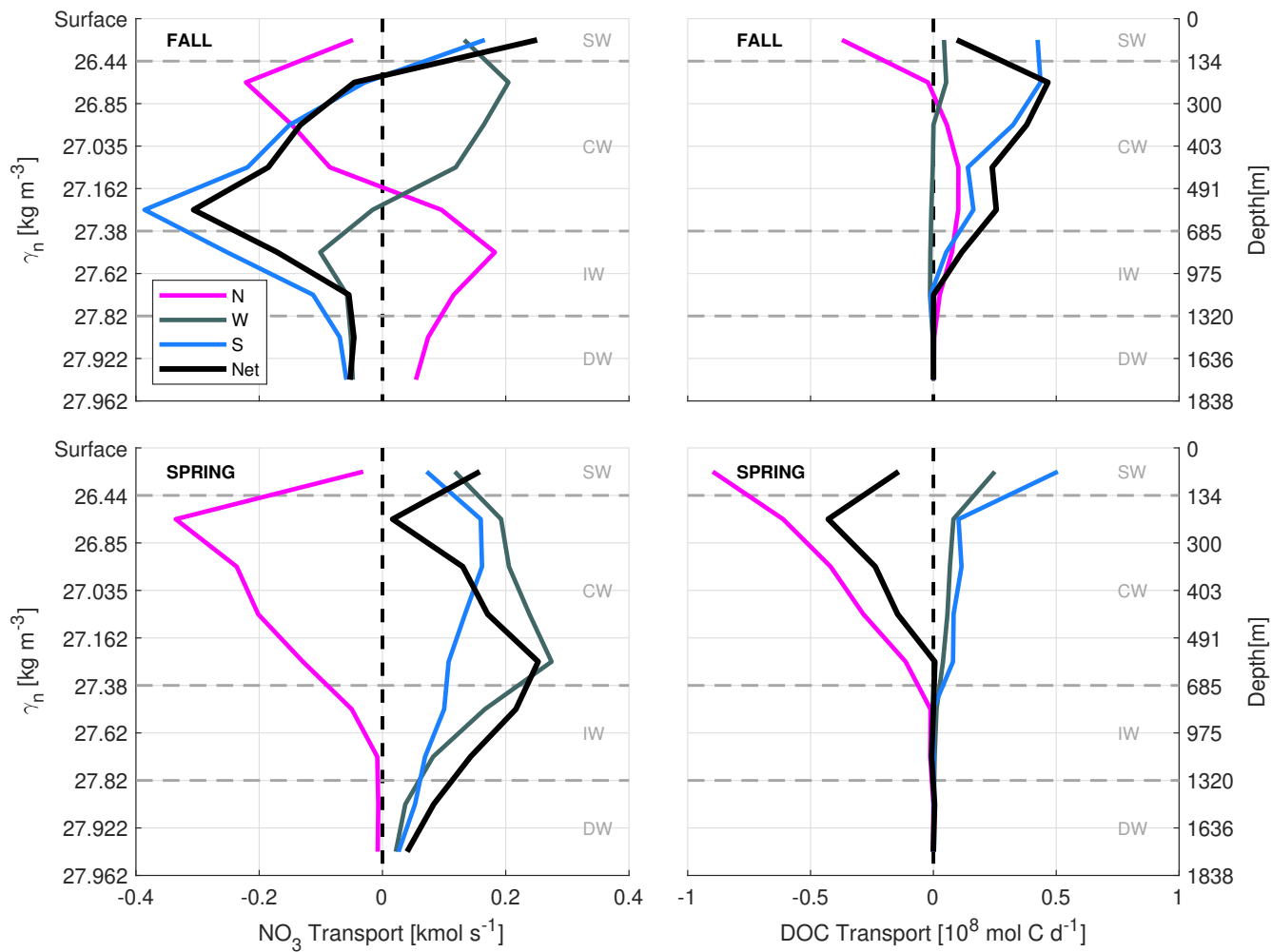
Figure 17. Accumulated NO_3 transports ($\mathrm{kmol\,s^{-1}}$) and accumulated DOC transports ($10^8\,\mathrm{mol\,C\,d^{-1}}$) at transects north (N, magenta line), west (W, dark grey line) and south (S, blue line) during fall (top) and spring (bottom). See Tab. 2 to check γ_n values bounding every water layer. Negative/positive values indicate inward/outward transports as in Fig. 12. The net transport in the whole box is shown by the black line.
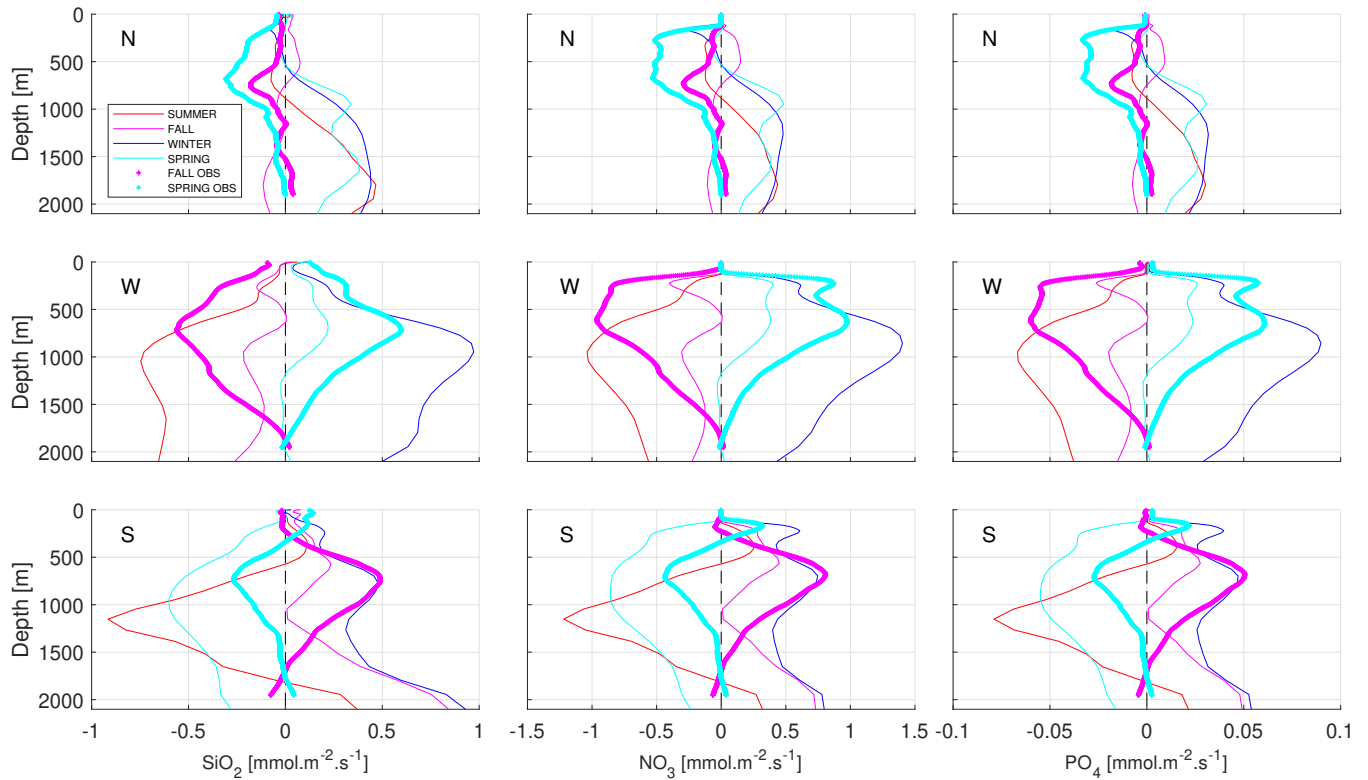
Figure 18. Numerical modelling of seasonal SiO_2 (left), NO_3 (center) and PO_4 (right) fluxes in $mmol.m^{-2}.s^{-1}$ at the three key points (N,in north transect, top; W, in west transect, center; and S, in south transect, down). There are represented: summer, from July to September, in red thin line; fall, from October to December, in magenta thin line; winter, from January to March, in blue thin line; and spring, from April to June, in cian thin line.They are also plotted the three nutrients fluxes observed *in situ* in fall (magenta) and spring (cian) with thicker dotted lines.

Table 1. Summary of the number and type of measurement in stations per transect and season.

SEASON [Cruise]	Type of measurement	Number of stations			
		North	West	South	Total
FALL [COCA-I]	CTD	14	6	11	29
	IN	8	2	6	14
	DOC	8	2	6	15
SPRING [COCA-II]	CTD	15	6	12	31
	IN	9	3	8	18
	DOC	10	3	7	18

Table 2. Summary of water levels (CW, IW, and DW) with their isoneutral limits and their water masses properties for both seasons from the sea surface to 2000 m. The properties extracted from observations are *in situ* temperature (T), potential temperature (θ), conservative temperature (Θ), practical salinity (S_P), absolute salinity (S_A), and dissolved organic carbon (DOC). IN extracted from GLORYS-BIO are silicates (SiO_2), nitrates (NO_3) and phosphates (PO_4).

WATER LEVELS		CW				IW				DW	
γ_n		MIN.		MAX.		MIN.		MAX.		MIN.	MAX.
[kg m^{-3}]		26.44		27.38		27.38		27.82		27.82	27.962
WATER MASSES		NACW		SACW		MW		AAIW		NADW	
PROPERTIES	SEASON	MIN.	MAX.	MIN.	MAX.	MIN.	MAX.	MIN.	MAX.	MIN.	MAX.
T	FALL	9.12	19.13	8.22	17.18	6.03	10.02	5.25	9.12	3.63	5.66
[°C]	SPRING	5.90	19.76	8.35	17.14	6.01	10.04	5.16	9.41	3.63	5.57
θ	FALL	9.04	19.11	8.14	17.16	5.90	9.94	5.13	9.05	3.46	5.53
[°C]	SPRING	5.77	19.74	8.27	17.13	5.88	9.96	5.06	9.34	3.47	5.45
Θ	FALL	9.03	19.05	8.13	17.12	5.89	9.92	5.12	9.03	3.46	5.53
[°C]	SPRING	5.77	19.67	8.26	17.09	5.88	9.94	5.05	9.32	3.47	5.44
S_P	FALL	35.23	36.83	35.04	36.19	35.13	35.44	34.92	35.24	34.99	35.13
	SPRING	33.85	37.06	35.07	36.16	34.55	35.53	34.96	35.30	34.99	35.12
S_A	FALL	35.40	37.00	35.21	36.36	35.30	35.61	35.09	35.40	35.16	35.30
[g kg^{-1}]	SPRING	34.02	37.23	35.24	36.33	34.72	35.70	35.13	35.47	35.16	35.30
SiO_2	FALL	1.24	18.46	6.39	22.14	13.23	21.73	17.50	25.78	18.94	28.44
[µmol kg^{-1}]	SPRING	1.22	21.99	6.99	23.95	13.97	21.99	17.97	28.06	19.04	28.73
NO_3	FALL	0.00	30.27	22.03	36.15	23.13	30.92	25.82	36.36	20.55	28.26
[µmol kg^{-1}]	SPRING	0.00	30.36	25.21	36.75	23.78	31.18	25.70	36.81	21.06	27.97
PO_4	FALL	0.03	1.90	1.46	2.29	1.43	1.98	1.69	2.33	1.37	1.85
[µmol kg^{-1}]	SPRING	0.03	1.90	1.69	2.36	1.49	1.98	1.69	2.39	1.42	1.83
DOC	FALL	47.85	108.65	49.05	74.13	46.25	66.09	41.83	59.30	41.82	58.72
[µM]	SPRING	41.66	105.62	40.86	63.45	40.44	65.15	40.44	50.17	40.44	50.81

Table 3. *A priori* noise of equations corresponding to SW, CW, IW and DW levels where the different water masses are transported.

WATER LEVELS	UNCERTAINTIES (Sv^2)
SW and CW	$(1.6 - 4.7)^2$
IW	$(6.3 - 9.3)^2$
DW	$(4.0 - 7.9)^2$

Table 4. Mass transports with their errors (Sv) for SW, CW, IW, and DW across north, west, and south transects for both seasons. Positive/negative values indicate outward/inward transports. The last row is the integrated transport for all the water column in each transect while the fourth column summarizes the imbalances in mass transport for both seasons.

WATER LEVELS	SEASON	NORTH	WEST	SOUTH	IMBALANCE
SW	Fall	-2.67 ± 0.60	2.46 ± 0.66	-0.50 ± 0.45	-0.71 ± 1.00
SW	Spring	-1.80 ± 0.49	1.09 ± 0.69	2.40 ± 0.53	1.70 ± 0.99
CW	Fall	-2.94 ± 1.26	3.50 ± 1.09	-3.85 ± 1.03	-3.29 ± 1.95
CW	Spring	-4.89 ± 1.14	2.96 ± 1.06	2.80 ± 1.02	0.87 ± 1.86
IW	Fall	1.94 ± 1.85	0.48 ± 1.71	-1.93 ± 1.69	0.49 ± 3.03
IW	Spring	-0.48 ± 1.65	1.21 ± 1.68	0.39 ± 1.73	1.1 ± 2.92
DW	Fall	0.73 ± 1.71	0.32 ± 1.56	0.19 ± 1.37	1.24 ± 2.69
DW	Spring	-0.04 ± 1.54	0.09 ± 1.53	0.00 ± 1.42	0.05 ± 2.59
TOTAL	Fall	-2.59 ± 2.88	6.99 ± 2.64	-5.82 ± 2.45	-1.43 ± 4.61
TOTAL	Spring	-7.24 ± 2.57	5.27 ± 2.60	5.53 ± 2.52	3.55 ± 4.44

Table 5. SiO_2 transports and their errors $(\mathrm{kmol\,s^{-1}})$ for CW, IW, and DW for north, west and south transects. Positive/negative values indicate outward/inward transports. The last row is the integrated transport in all the water column in each transect and the last column represents the net transport for this variable inside the box.

WATER LEVELS	SEASON	NORTH	WEST	SOUTH	IMBALANCE
SW	Fall	-0.06 ± 0.01	0.06 ± 0.02	0.02 ± 0.02	0.02 ± 0.02
	Spring	-0.06 ± 0.02	0.04 ± 0.02	0.06 ± 0.01	0.04 ± 0.02
CW	Fall	-0.14 ± 0.06	0.21 ± 0.06	-0.41 ± 0.11	-0.34 ± 0.20
	Spring	-0.40 ± 0.09	0.45 ± 0.16	0.23 ± 0.08	0.28 ± 0.61
IW	Fall	0.23 ± 0.22	-0.13 ± 0.45	-0.27 ± 0.24	-0.17 ± 1.07
	Spring	-0.04 ± 0.15	0.19 ± 0.27	0.12 ± 0.55	0.28 ± 0.72
DW	Fall	0.13 ± 0.31	-0.11 ± 0.52	-0.14 ± 1.00	-0.12 ± 0.25
	Spring	-0.01 ± 0.51	0.06 ± 1.15	0.08 ± 13.38	0.13 ± 6.79
TOTAL	Fall	0.16 ± 0.17	0.03 ± 0.01	-0.80 ± 0.34	-0.61 ± 1.97
	Spring	-0.51 ± 0.18	0.75 ± 0.37	0.49 ± 0.22	0.73 ± 0.91

Table 6. NO_3 transports and their errors ($\mathrm{kmol\,s^{-1}}$) for CW, IW, and DW for north, west and south transects. Positive/negative values indicate outward/inward transports. The last row is the integrated transport in all the water column in each transect and the last column represents the net transport of this variable inside the box.

WATER LEVELS	SEASON	NORTH	WEST	SOUTH	IMBALANCE
SW	Fall	-0.05 ± 0.01	0.13 ± 0.04	0.17 ± 0.15	0.25 ± 0.35
SW	Spring	-0.03 ± 0.01	0.12 ± 0.07	0.07 ± 0.02	0.16 ± 0.09
CW	Fall	-0.36 ± 0.15	0.47 ± 0.15	-0.78 ± 0.21	-0.67 ± 0.40
CW	Spring	-0.90 ± 0.21	0.91 ± 0.33	0.56 ± 0.20	0.57 ± 1.22
IW	Fall	0.30 ± 0.28	-0.16 ± 0.57	-0.36 ± 0.32	-0.23 ± 1.39
IW	Spring	-0.06 ± 0.20	0.25 ± 0.35	0.17 ± 0.75	0.36 ± 0.94
DW	Fall	0.13 ± 0.30	-0.10 ± 0.48	-0.13 ± 0.91	-0.10 ± 0.21
DW	Spring	-0.01 ± 0.52	0.06 ± 1.05	0.08 ± 12.63	0.12 ± 6.26
TOTAL	Fall	0.02 ± 0.02	0.35 ± 0.13	-1.11 ± 0.47	-0.74 ± 2.40
TOTAL	Spring	-1.01 ± 0.36	1.34 ± 0.66	0.88 ± 0.40	1.21 ± 1.51

Table 7. PO_4 transports and their errors $(\mathrm{kmol\,s^{-1}})$ for CW, IW, and DW for north, west and south transects. Positive/negative values indicate outward/inward transports. The last row is the integrated transport in all the water column in each transect and the last column represents the net transport of this variable inside the box.

WATER LEVELS	SEASON	NORTH	WEST	SOUTH	IMBALANCE
SW	Fall	-0.00 ± 0.00	0.01 ± 0.00	0.01 ± 0.01	0.02 ± 0.02
	Spring	-0.00 ± 0.00	0.01 ± 0.01	0.01 ± 0.00	0.01 ± 0.01
CW	Fall	-0.02 ± 0.01	0.03 ± 0.01	-0.05 ± 0.01	-0.04 ± 0.02
	Spring	-0.06 ± 0.01	0.06 ± 0.02	0.04 ± 0.01	0.04 ± 0.08
IW	Fall	0.02 ± 0.02	-0.01 ± 0.04	-0.02 ± 0.02	-0.01 ± 0.09
	Spring	-0.00 ± 0.01	0.02 ± 0.02	0.01 ± 0.05	0.02 ± 0.06
DW	Fall	0.01 ± 0.02	-0.01 ± 0.03	-0.01 ± 0.06	-0.01 ± 0.01
	Spring	-0.00 ± 0.04	0.00 ± 0.07	0.01 ± 0.85	0.01 ± 0.42
TOTAL	Fall	0.00 ± 0.00	0.02 ± 0.01	-0.07 ± 0.03	-0.05 ± 0.15
	Spring	-0.06 ± 0.02	0.08 ± 0.04	0.06 ± 0.03	0.08 ± 0.10

Table 8. DOC transports and their errors ($10^8\,\mathrm{mol\,C\,d^{-1}}$) for CW, IW, and DW for north, west and south transects. Positive/negative values indicate outward/inward transports. The last row is the integrated transport in all the water column in each transect and the last column represents the net transport for this variable inside the box. These values are transports of non-refractory DOC which is obtained by subtracting an amount of $40\,\mathrm{\mu mol\,L^{-1}}$ from the measured DOC.

WATER LEVELS	SEASON	NORTH	WEST	SOUTH	IMBALANCE
SW	Fall	-0.37 ± 0.08	0.04 ± 0.01	0.42 ± 0.38	0.10 ± 0.13
SW	Spring	-0.90 ± 0.24	0.25 ± 0.16	0.51 ± 0.11	-0.14 ± 0.08
CW	Fall	0.24 ± 0.10	0.04 ± 0.01	1.06 ± 0.28	1.34 ± 0.80
CW	Spring	-1.43 ± 0.33	0.25 ± 0.09	0.38 ± 0.14	-0.80 ± 1.72
IW	Fall	0.10 ± 0.10	-0.03 ± 0.09	0.04 ± 0.04	0.12 ± 0.72
IW	Spring	-0.02 ± 0.08	0.02 ± 0.02	-0.00 ± 0.00	-0.01 ± 0.02
DW	Fall	0.00 ± 0.01	-0.00 ± 0.02	-0.00 ± 0.00	0.00 ± 0.00
DW	Spring	-0.00 ± 0.06	0.00 ± 0.04	0.00 ± 0.58	0.00 ± 0.23
TOTAL	Fall	-0.03 ± 0.03	0.06 ± 0.02	1.53 ± 0.64	1.55 ± 5.01
TOTAL	Spring	-2.35 ± 0.84	0.52 ± 0.25	0.89 ± 0.40	-0.95 ± 1.19